Carbon Nano-Material Based Saturable Absorbers and their Application to Mode-Locked Lasers

Christopher Young Rodenchuk

Department of Electrical & Computer Engineering
McGill University
Montreal, Canada

May 2011

Under the supervision of Professors Lawrence Chen and Thomas Szkopek

---

A thesis submitted to McGill University in partial fulfillment of the requirements for the degree of Master of Engineering.

Abstract

The first part of this thesis presents the implementation of a passively mode-locked fiber ring laser incorporating single walled carbon nanotubes (SWNT). The laser was found to generate soliton pulses with pulsewidths on the order of 1 ps and bandwidths of 3.5 nm at a repetition rate of 10 MHz. Power dependent harmonic mode-locking was demonstrated, generating pulses with a repetition rate of up to 130 MHz.

The second part of the thesis presents an attempt to determine if carbon nanoparticles, known as carbon black, exhibit similar nonlinear optical properties to other forms of carbon nano-materials, making them suitable for use in mode-locked lasers. The nonlinear measurements were inconclusive, however a Q-switched laser was demonstrated incorporating carbon black. The laser had power dependent pulsewidths on the order of 10 us, repetition rates on the order of 27 kHz and was wavelength tuneable in the region of 1545 to 1565 nm.

Abrégé

La première partie de cette thèse présente l'implémentation des lasers en anneau de fibres en mode passivement bloqué incorporant des nanotubes à paroi simple (SWNT). Le laser a généré des impulsions de solitons avec des largeur d'impulsions de l'ordre de la picoseconde et des bandes passantes de 3.5nm à une fréquence de répétition de 10 MHz. La démonstration de la dépendance en puissance en mode bloqué harmonique à été faite en générant des impulsions avec des fréquences de répétition jusqu'à 130 MHz.

La deuxième partie de cette thèse présente une tentative afin de démontrer si les nanoparticules de carbone, aussi nommée noir de carbone, démontre des propriétés optiques non-linéaires similaires aux autres formes de nano-matériaux de carbone, ce qui peut les rendre utile dans des lasers à mode bloqué. Les mesures non-linéraires ont été inconclusives, mais un laser Q-switché fût démontré en utilisant le noir de carbone. Le laser avait des largeurs d'impulsions dépendante de la puissance de l'ordre de 10 us avec des fréquence de répétition autour de 27 kHz et peut être ajusté en longueur d'onde de 1545 à 1565 nm.

Acknowledgments

First and foremost, I would like to thank my supervisors Professors Lawrence Chen and Thomas Szkopek for their support, encouragement and guidance. I would also like to thank my lab mates, specifically Tommy Cai and Shaz Taslimi for their encouragement and good humor, Adrian for numerous coffee breaks and Karim for helping me print this thesis. Also all the peeps in 608.

I would like to thank my Mom for many things including letting me sleep in the spare room and my sister for eating all of my cookies. Also the two dogs and a cat that won't leave me be.

Contents

List of Figures

Chapter 1

Introduction

1.1 Saturable Absorbers and Mode-Locked Lasers

Lasers have become one of the most versatile tools used in the fields of science and engineering. They are being used in applications as varied as measuring distances in surveying, to attempting to fuse hydrogen atoms at the U.S. National Ignition Facility, as well as everything in between. Pulsed laser sources have proved to be indispensable; in particular, they are used in the transmission of information over long distances which has helped to drive the information age. Pulses capable of delivering huge amounts of energy to very small areas have revolutionized manufacturing, and short duration pulses have made advances in high speed imaging possible. Pulsed sources are generated using three basic methods: Q-switching, gain switching and mode-locking. The focus of this thesis is the mode-locked laser (MLL).

MLL's are primarily designed to generate ultra-short duration pulses of light. Passively MLL's in particular can achieve pulse widths on the order of a few femtoseconds [12, 13] and can have peak power on the order of kW's [14]. They are an ongoing

and active field of research. Ultra-short and high power pulses have found many applications in a wide array of fields including, observing chemical reactions on extremely short time scales using soft x-rays in the 4 to 40 nm wavelength range. Micromachining with short ultraviolet (UV) wavelengths in the 300 nm range, through photochemical reactions can achieve very fine feature sizes, while laser ablation processes take advantage of a variety of wavelengths ranging from the UV through 10.6 μm CO_2 lasers. Medical imaging has also made great use of MLL's, typical wavelengths range from the visible to 900 nm, or the near infrared (NIR). Ultra-short pulses have been used in terahertz generation, as well as Doppler free precision spectroscopy which both employ a wide range of IR frequencies. High repetition rate MLL's have many applications in high capacity telecommunication and optical communications systems and photonic switching devices which use the telecom C-band, centered at 1550 nm.

MLL's come in two varieties, actively and passively mode-locked. While actively MLL's employ an active modulation of the light within a laser cavity to develop a pulsed output, passively MLL's take advantage of a material property known as saturable absorption. Saturable absorbers (SA) are intensity dependent nonlinear optical devices. The defining characteristic of the SA is that its absorption decreases with increasing input light intensity. While sometimes employed in optical regeneration schemes [15], all optical switching [16], optical pulse shaping and for noise suppression [17], they are predominantly used as passive components in MLL's.

SA's can best be understood by considering a simple two state system with a ground state and an excited state. When a photon of sufficient energy impinges upon the system, a carrier is induced to jump the band gap. The carrier then typically de-excites at a given rate through thermalization back to the ground state. Under a

strong excitation with a sufficiently large number of photons, a material may exhibit saturation due to the depletion of ground state carriers. This can be modeled with a simple rate equation. In theory, any material can exhibit saturable absorption; however, in practice, heat build up due to thermalization will damage most materials before saturation is observed.

The earliest report of mode-locking with a SA was by Mocker and Collins in 1965 [18] using a rhodamine based organic dye. They were able to achieve pulse widths on the order of 10 ns. By 1966 DeMaria *et al.* [19] had achieved pulse widths on the order of picoseconds. By 1986 Valdmanis *et al.* [20] had demonstrated pulses as short as 27 fs directly from a laser oscillator. Organic dyes remained the dominant SA medium used in MLL's up until the late 1980's, but they suffered from a number of limitations. Q-switching, a long lived modulation of the pulse train which is due to a combination of long and short excitation lifetimes, can lead to a lack of regular pulses. Dyes also suffer from wavelength limitations and are typically only effective in the visible and NIR. Low damage thresholds are also a concern in light sensitive organic dyes which leads to power constraints and short device lifetimes. Dyes are also often highly toxic; this, in combination with the need to frequently replace short lifetime dye cells makes them particularly unwieldy.

By the early 1990's, advances in semiconductor growth processes and band gap engineering led to the development of the semiconductor saturable absorber mirror (SESAM) [21]. These devices employ multiple quantum well (MQW) structures or quantum dot structures that allow for precise band gap control, thermalization processes on the order of 10's to 100's of fs, and can be robustly designed for long device lifetimes. Depending on the semiconductor material used and the device geometry,

SESAM's can be fabricated to operate in the NIR out to the 1550 nm C-band for telecom applications. Individual SESAM's can also be tuneable over 100's of nm. SESAM's do, however, have the drawback that they are expensive to fabricate, require expensive clean room equipment and often have low damage thresholds.

In 2004, Set *et al.* [5] demonstrated the first example of a saturable absorber incorporating carbon nanotubes (SAINT) used to build a MLL. Since then, carbon based SA's have been a very active field of research. Both carbon nanotubes (CNT), quasi 1-Dimensional carbon rods, as well as graphene, single atom thick planar layers of carbon, have been shown to be highly promising SA's [4]. The band gap in carbon nanotubes has been shown to be widely tuneable, while graphene is a zero band gap semiconductor whose absorption spectrum is extremely broad. Both have been shown to have a slow and fast component to their recovery times, making them ideally suited to building a self starting MLL, and both are environmentally robust and have relatively large damage thresholds. Carbon nanotube growth techniques have reached a stage of maturity that makes CNT based SA's a more cost effective alternative to SESAM's, and bulk produced CNT's can be manipulated without the need for expensive equipment and clean room facilities.

1.2 Thesis Motivation

With the recent discovery that CNT and graphene based SA's are suitable for mode-locking of lasers, there was an interest in determining if other forms of carbon nanomaterial could be used to build MLL's. With this in mind we decided to investigate the possibility that carbon nanoparticles, known as carbon black, might also exhibit saturable absorption. There has been limited research on the nonlinear optical prop-

erties of carbon black, most of it centered on carbon black as an optical limiting agent when mixed in solution [22]. Carbon black offers a number of advantages over both graphene and SWNT's. It is easier and cheaper to produce in bulk then both graphene and SWNT's, it is easy to manipulate and does not require clean room equipment. Carbon black has the potential to be a low cost alternative to other carbon based MLL's. Finally, we were interested in characterizing a MLL built using SWNT given that this has been such a hot topic of research as of late.

1.3 Thesis Outline

Chapter 2 of this thesis will present background theory associated with the various allotropes of carbon used in this set of experiments. A brief introduction to carbon-carbon bonding will be given, followed by a discussion of the optical properties of graphene and SWNT's. The structure of carbon black will be explained and a justification for the belief that they are a SA material will be given.

Chapter 3 presents the implementation of a fiber ring MLL using SWNT's.

Chapters 4 presents the experiments performed using carbon black. Specifically, the linear and nonlinear absorption will be measured in air and in vacuum and the results will be given. Also an experiment involving carbon black as an electron source, which led to a report of invention being filed with McGill's Office of Technology Transfer, will be discussed. Carbon black will be used in a ring laser configuration to implement a passively Q-switched laser.

In chapter 5 the work will be summarized and a brief conclusion of the results given along with a description of possible further work.

Chapter 2

Background

Section 1 of the background briefly discuss both active and passive mode-locking, and presents a mathematical model for MLL's involving SA's. A model for a SA is also given and discussed.

Section 2 gives an overview of carbon allotropes and carbon-carbon bonding. In particular the bonds leading to the formation of graphene, graphite and nanotubes will be discussed.

Section 3 discusses the optical properties of both SWNT's and graphene. Experimental results for the linear and nonlinear optical absorption are shown as well as the time dynamics of saturation. Finally, a motivation for the hypothesis that carbon black is a SA is given.

Section 4 provides a brief overview of the current state of research involving MLL incorporating SWNT's.

2.1 Laser Mode-Locking with Saturable Absorbers

In general, Continuous Wave (CW) lasers consist of a resonant cavity, which functions as a feedback mechanism, and a gain medium. All laser cavities also have losses, both material losses in the cavity medium and coupling losses at the laser output. MLL's are built using a periodic modulation of the cavity losses. There are two categories of MLL's, actively modulated and passively modulated. Actively modulated MLL's involve a lossy element within the cavity whose loss can be controlled externally. By modulating the loss in a periodic fashion, the laser can be made to pulse. Passively MLL's include a lossy element whose loss is modulated by the intensity of light impinging on it, a SA. The SA promotes higher energy pulses while suppressing lower energy signals, leading to a pulsed mode of operation.

Conceptually, it is helpful to consider an actively MLL, which is schematically shown in figure 2.1 A, where the cavity losses are modulated with a period equal to the round trip time T_R of the laser cavity. If we start with a CW signal traveling within the cavity, and decrease the losses seen by one temporal envelope of the signal within one part of the cavity on each round trip, it is easy to visualize the steady build up of a pulse within the cavity.

In the frequency domain, the optical cavity resonator has axial modes separated in frequency by $\Delta\Omega = \frac{2\pi}{T_R}$, figure 2.1 B. With no loss modulation, power within the cavity will build until the gain saturates, which is to say that the round trip increase in power due to the gain medium equals the round trip losses in the cavity. The cavity gain is clamped to the cavity losses and very few axial modes will lase, this is shown as the free running gain, and leads to a steady state CW operation. By applying a periodic loss modulation, we can increase the gain seen by a number of modes. The

loss modulation effects the locking of modes by coherent coupling in frequency space, or imparting a pulse shape in the time domain.

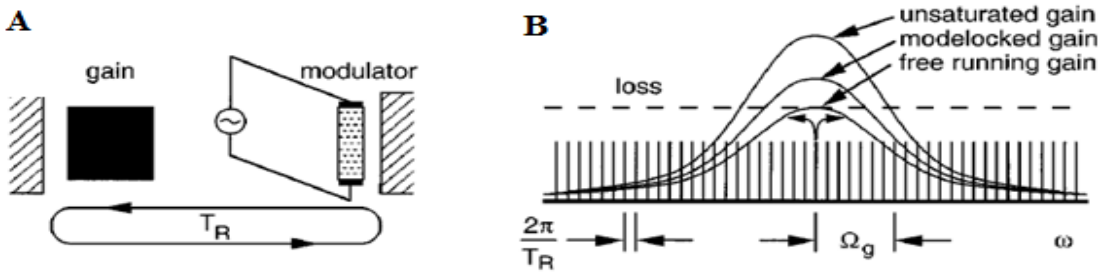

Fig. 2.1 A, Laser cavity showing the gain medium and loss modulator. B, Axial modes and gain loss spectrum.[1]

In steady state, the pulses from an actively MLL can be modeled using the Haus master mode-locking equation [1]

$$\frac{1}{T_R}\frac{d}{dT}a(T,t) = (g-l)a(T,t) + \frac{g}{\Omega_g^2}\frac{d}{dt}^2 a(T,t) - \frac{1}{2}M{\Omega_m}^2 t^2 a(T,t) \tag{2.1}$$

where a is the pulse envelope which is a function of both time τ and a long term time variable T which develops on the order of T_R, g is the saturated gain co-efficient and Ω_g is related to the gain bandwidth and l is the unsaturated loss. The last term in equation 2.1 represents the active periodic modulation of the cavity losses with M being the modulation depth and Ω_m is the modulation frequency. This equation uses a second order expansion of the frequency dependent gain and assumes a very dense frequency spectrum.

The passive loss modulation provided by the SA can be modeled as

$$s(t) = \frac{s_0}{(1 + I(t)/I_{sat})} \tag{2.2}$$

where $s(t)$ denotes the absorption, s_0 (<1) is the unsaturated loss, $I(t)$ is the time dependent intensity, and I_{sat} is the saturation intensity, related to the intensity required to observe a change in absorption.

The power in the signal can be determined by multiplying the intensity of the pulse by the effective area A_{eff}, which is defined to be a measure of the area which the pulse covers in the transverse dimension. If we assume a relatively weak saturation and normalize the mode amplitude such that $|a(t)|^2 =$ power, we get

$$s(t) = s_0 - \frac{(s_0|a(t)|^2)}{(I_{sat}A_{eff})} \equiv s_0 - \gamma|a(t)|^2 \tag{2.3}$$

where γ is the self amplitude modulation (SAM) coefficient, and is related to the slope of the power vs absorption characteristic of the SA.

By replacing the active modulation term in the master equation with the passive term just derived, and lumping the unsaturated loss coefficient in with the cavity loss l, we arrive at the passively mode-locked equation [1]

$$\frac{1}{T_R}\frac{d}{dT}a = (g-l)a + \frac{g}{\Omega_g^2}\frac{d}{dt}^2 a + \gamma|a(t)|^2 a \tag{2.4}$$

The solution to equation 2.4 is the hyperbolic secant given in equation 2.5.

$$a_0(t) = A_0 sech(t/\tau) \tag{2.5}$$

with

$$\tau^2 = \frac{g}{(l-g)\Omega_g^2} \tag{2.6}$$

and

$$A_0{}^2 = \frac{2g}{\tau^2 \Omega_g^2 \gamma} \tag{2.7}$$

We would expect the power output of a passively MLL to take on a $sech^2$ profile.

For a more rigorous treatment of the mode-locking of lasers, see the theory derived by Herman Haus [1], and for a full time domain treatment of passively MLL's see [23].

Turning back to the simple SA model, if we consider a strong saturation, we need to include a parameter b_0 that accounts for the non-saturable losses present in the material, typically due to scattering. This results in equation 2.8.

$$a(I) = b_0 + \frac{s_0}{(1 + I/I_{sat})} \tag{2.8}$$

Normalizing the absorption such that $s_0 + b_0 = 1$ and plotting this function gives figure 2.2, where Sat indicates the point at which the absorber is fully saturated and γ is the SAM coefficient.

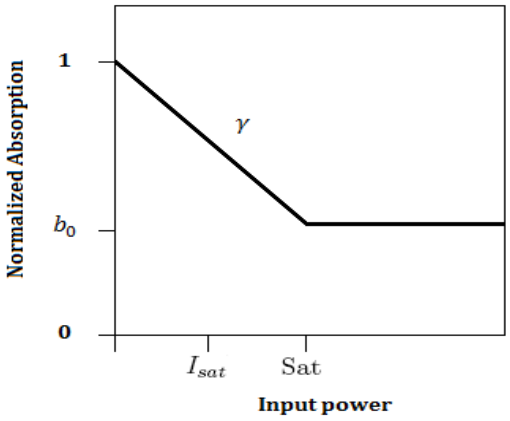

Fig. 2.2 The absorption characteristic of an idealized SA.

Generally, MLL's are ideally suited to generate high intensity, ultra short pulses. With this in mind we can consider some of the important characteristics of a SA. The SA has a mode-locking effect as previously described, but also has a pulse shaping effect. This is due to the SA more strongly attenuating the leading edge of the pulse, which has lower intensity, than the peak of the pulse which has the highest optical intensity. Depending on the recovery time, which is defined as the time required for the absorber to return to its unsaturated absorption once a pulse has passed, it may also attenuate the trailing edge of the pulse. A fast SA is one in which the recovery time is significantly shorter than the pulse width. For the purpose of generating a short pulse, a fast SA is desirable as this will result in strong pulse shaping. The modulation depth is defined as the maximum possible change in the absorption; it is equal to s_0. A large modulation depth leads to strong pulse shaping, as the attenuation seen by the edges of the pulse will be large compared to the attenuation seen by the peak of the pulse. The saturation intensity is defined as the input optical intensity required to reduce the saturable absorption to half of its small signal value. In general a low saturation intensity is preferable as this facilitates mode-locking at lower powers, however, for high power lasers a higher saturation intensity is desirable. Taken together, a large modulation depth and small saturation intensity imply a large SAM coefficient.

2.2 Carbon

Carbon is among the oldest of the known elements, having been used since antiquity as a fuel and as a catalyst for producing bronze. Antoine Lavoisier first listed carbon as an element in his book, Traité Élémentaire de Chimie, published in Paris in 1789. Three allotropes of carbon, diamond, graphite and amorphous carbon have

been known and used throughout written history. In 1985, Kroto *et al.* discovered another allotrope of carbon which they called the Buckminsterfullerene [24]. This discovery won them the 1996 Nobel Prize in chemistry. The discovery of fullerenes sparked an increasing interest in carbon nanostructures. In 1991 Iijima [25] produced the first transmission electron microscope (TEM) images of carbon nanotubes, and reported on a catalyst free method of growth. This discovery is generally credited with catapulting the carbon nanotube into the main stream of scientific research. In 2004 researchers at the University of Manchester published a paper on the electronic properties of atomic layer graphene [26], and introduced the first method by which graphene was widely produced. For their discovery the authors, Geim and Novoselov, were awarded the 2010 Nobel prize in physics.

The wide variety of polymorphism of carbon is due to its unique electronic configuration, which allows for a number of hybridized atomic orbitals. The carbon atom has two $1s$ orbitals, two $2s$ orbitals and six $2p$ orbitals. While the inner shell $1s$ orbitals are not available to form bonds, all of the valence shell $2s$ and $2p$ orbitals are. The $2s$ and $2p$ orbitals of the carbon atom have similar energies, and as such can easily hybridize. The process of hybridization involves an overlap of the wavefunction of the s and p orbitals leading to the hybridized orbitals shown in figure 2.3.

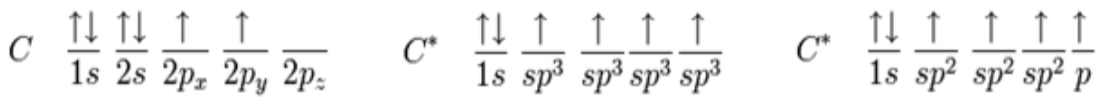

Fig. 2.3 C is the ground state of the carbon atoms electronic configuration, C*'s are the $sp2$ and $sp3$ hybridized orbital.

The allotropes of carbon are all formed using two sets of hybridized covalent bonds, the $sp2$ and $sp3$ bonds.

An $sp3$ hybridized bond involves the overlap of one s orbital with three p orbitals. A carbon atom can share four such bonds, leading to a tetrahedral structure with four nearest neighbours. The four sigma (σ) bonds of equal length involve all orbitals and electrons. This is carbon's diamond structure. In this configuration all electrons are tightly bound to carbon atoms and as such do not interact strongly with visible or IR light, leading to diamond being transparent over a broad frequency spectrum.

The $sp2$ hybridized bonds involve the overlap of one s orbital with two p orbitals. A carbon atom can share three such bonds, leading to a planar triangular structure. The three σ bonds of equal length involve all but one p orbital electron. This planar configuration leads to the formation of a number of carbon allotropes including graphite, graphene, Buckminsterfullerenes and carbon nanotubes.

The p orbital electron can occupy a broad range of energy and momentum states, and as a result interacts strongly with a broad range of electromagnetic radiation, leading to these carbon allotropes appearing very dark in colour as little light is transmitted or reflected.

The delocalized p orbital electron in the planar configuration leads to a wide variety of electronic and optical properties. Graphene is a truly 2-dimensional crystal structure. The interactions between the electrons and the graphene lattice cause the electrons to act as though they have no mass, and as a result are governed by the Dirac equation [27] leading to exceptionally high mobilities. The energy states within the lattice allow for a broad range of electrical transitions; this in combination with its small thickness in the transverse direction leads to a low density of states. Considering this low density of states, it is possible to pump the material hard enough to excite all the carriers at the pump wavelength, thereby reducing the electron light interaction,

while not pumping so hard as to damage the material. This is the basis for saturable absorption in graphene and carbon nano-materials in general.

2.3 Graphene and SWNT optical absorption characteristics.

2.3.1 Linear Absorption

The linear optical absorption spectrum of graphene in the visible and infrared regions has been calculated to be independent of wavelength and have a magnitude equal to $\pi\alpha$, where α is the fine structure constant $\frac{e^2}{\hbar c}$ [28]. This result has been experimentally verified [2], figure 2.4.

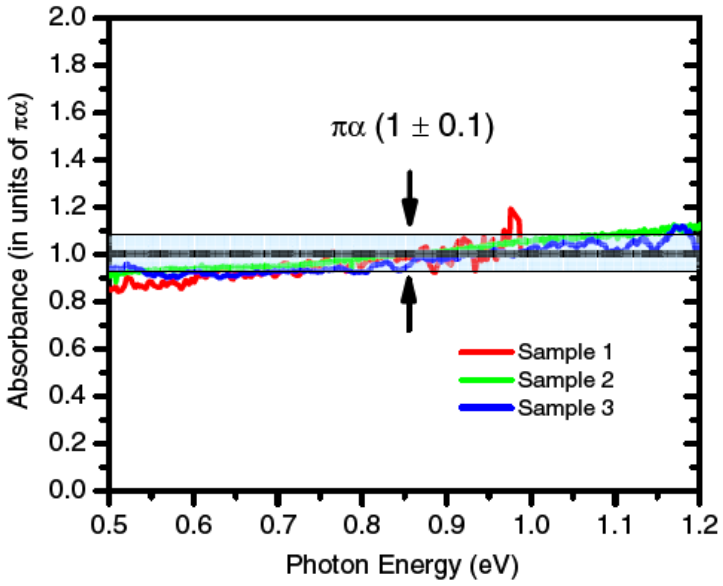

Fig. 2.4 Optical absorbance of graphene in the visible and IR [2].

The absorption associated with p orbital electrons is nearly invariant in frequency. As a result, we would expect graphene to make an excellent broadband saturable

absorber.

Viewing a SWNT as a rolled up, seamless tube of graphene, we can think of SWNT's as a quasi 1-dimensional structure, similar to graphene with an added degree of quantum confinement. This leads to a restriction on the energy states that the p orbital electrons can assume, resulting in the absorption characteristic seen in figure 2.5 [3].

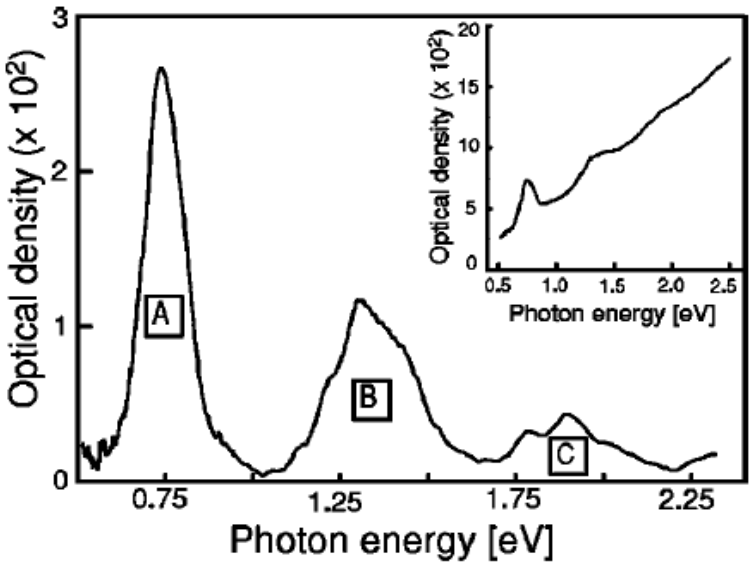

Fig. 2.5 Typical optical absorption spectrum of SWNT after background correction, inset shows raw data [3].

The p orbital electrons in SWNT's are restricted to excitations at the energy levels labelled A, B and C. As a result SWNT's, will absorb photons strongly at these energy levels while being almost transparent at other energy levels. The positioning and magnitude of these absorption peaks is strongly dependent on both the radius of the individual tubes and their chirality. Smaller diameter tubes will have their

peaks shifted to higher energy levels, while absorption peaks of larger diameter tubes will shift to lower energies. This characteristic of SWNT's allows for the tailoring of optical absorption spectra using different SWNT growth parameters and techniques, allowing for the engineering of CNT based SA's across a broad range of frequencies.

2.3.2 Nonlinear absorption

Saturable absorption in graphene was experimentally verified by Bao *et al.* [4] in 2009.

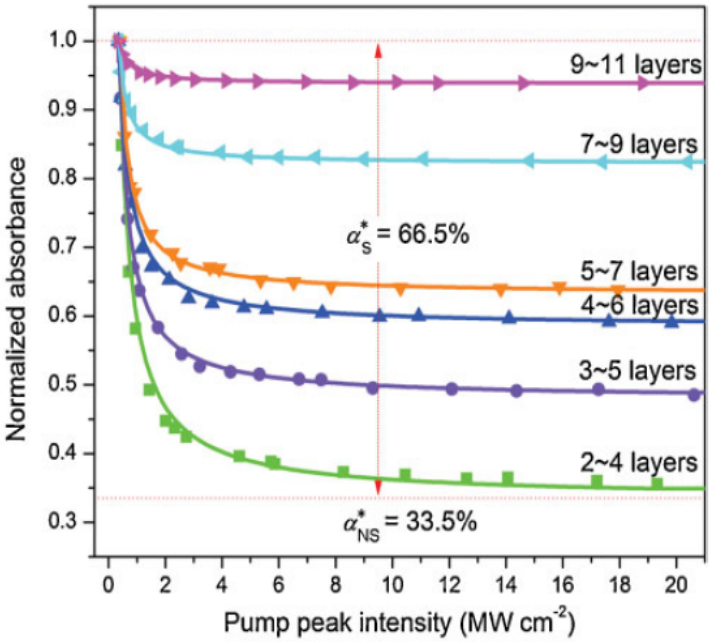

Fig. 2.6 Saturable absorption of various thicknesses of graphene [4].

In figure 2.6, taken at 1550 nm, the telecommunications wavelength, we see that graphene composed of approximately 8 layers has a modulation depth greater than 10%. This approaches a modulation depth of 70% for bilayer graphene, with a sat-

uration intensity of around 1 $^{MW}/_{cm^2}$. As the number of layers increases, the modulation depth decreases monotonically. In principle, this allows for the tailoring of the modulation depth simply by increasing the number of layers. This has important implications as a small modulation depth SA can be desirable depending on the type of laser being built and its application. We can deduce from the graph that as the number of layers continues to increase the material will eventually no longer exhibit saturable absorption, as is the case for macroscopic graphite.

Saturable absorption in SWNT was confirmed in 2004 by Set *et al.* [5].

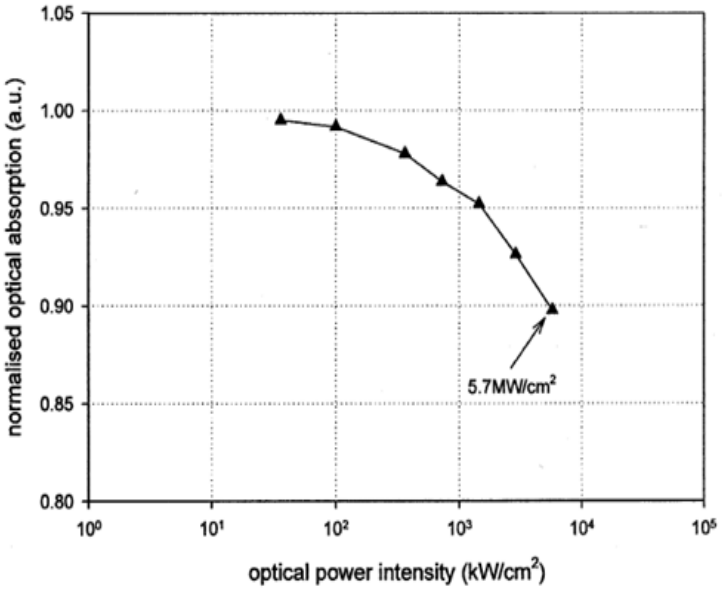

Fig. 2.7 Normalized absorption of SWNT's as a function of peak optical power intensity [5].

The graph in figure 2.7 was also made using telecommunication wavelengths. For this type of SWNT we see a slightly higher saturation intensity than in the case of graphene, which in general is the case. Higher saturation intensity can be desirable,

as power within a laser cavity can be quite large. In high power applications, higher saturation intensities can lead to lower noise in the laser output. The modulation depth cannot be deduced from the graph as the maximum optical power is not high enough; however, SWNT have been shown to have modulation depths on the order of 20% [29].

2.3.3 Recovery Times

The recovery time of graphene has been measured [6] and is shown in figure 2.8.

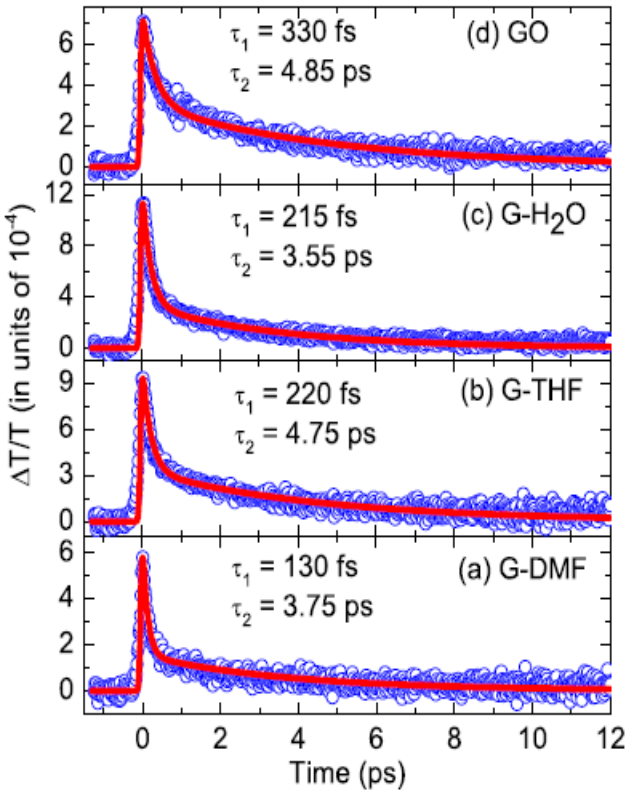

Fig. 2.8 Recovery times of graphene in different solvents [6].

When graphene is suspended in solution, its p orbital electrons will interact with the surrounding material, leading to slightly different carrier dynamics and slightly different recovery times which are evident in figure 2.8. We also note that there are two distinct time constants, a fast and a slow component to the recovery time. This again is a feature of the carrier dynamics and it is not unique to graphene. The two carrier relaxation times can be advantageous as the fast response will lead to strong pulse shaping and shorter pulse widths, while the slow response will help with the self starting of a MLL's, whereby the laser will spontaneously begin to mode-lock once a critical threshold power is reached. The fast recovery time of graphene is on the order of a few hundreds of fs, down to 130 fs, indicating that it would be an ideal SA for generating sub ps pulses.

The recovery time of SWNT's has been measured [7].

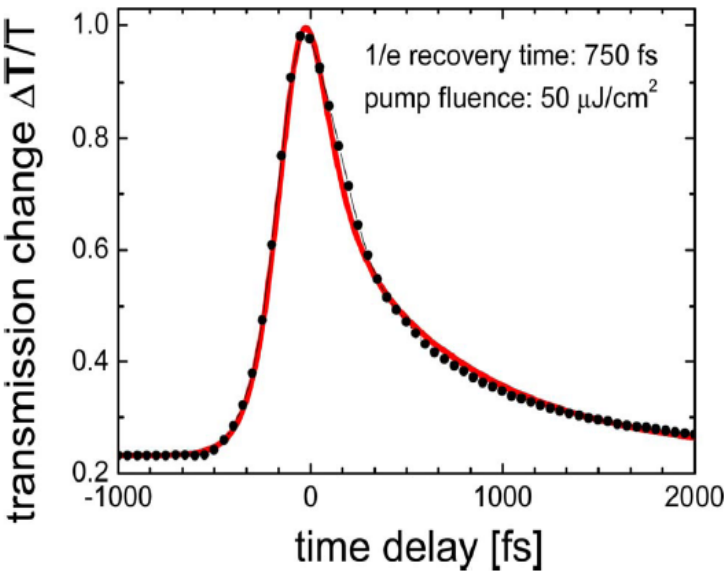

Fig. 2.9 Recovery time of SWNT [7].

SWNT's typically have recovery times on the order of 600 to 800 fs or longer. This is sufficient to generate ultrafast pulses but with less strong pulse shaping than with graphene.

2.3.4 Carbon Black

Carbon black is essentially comprised of poorly crystallised spherical particles formed by an assembly of microcrystallites. These particles are highly disordered at the center, but tend towards an 'onion peel' structure at the surface [30]. The interlayer spacing between graphene sheets is a minimum of around 350 pm, but can be much larger due to disorder in the layered structure. A transmission electron microscope (TEM) image is shown in figure 2.10 [8].

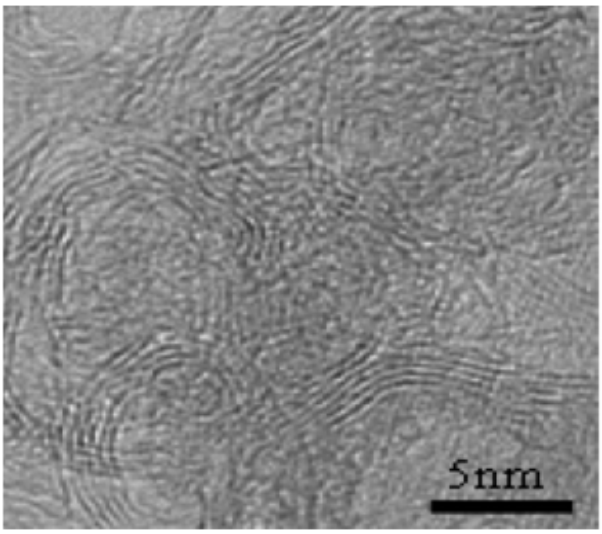

Fig. 2.10 Typical high resolution image TEM image of carbon black [8].

As we have seen, individual semiconducting graphene sheets exhibit strong saturable absorption, whereas semi-metallic graphite does not. The motivation for look-

ing for saturable absorption in carbon black stems from the observation that carbon black may represent one of the intermediate stage between graphene and graphite.

2.4 Mode-Locked Lasers incorporating SWNT's

The first reported MLL's incorporating CNT's [5] employed the fiber ring laser configuration shown in figure 2.11.

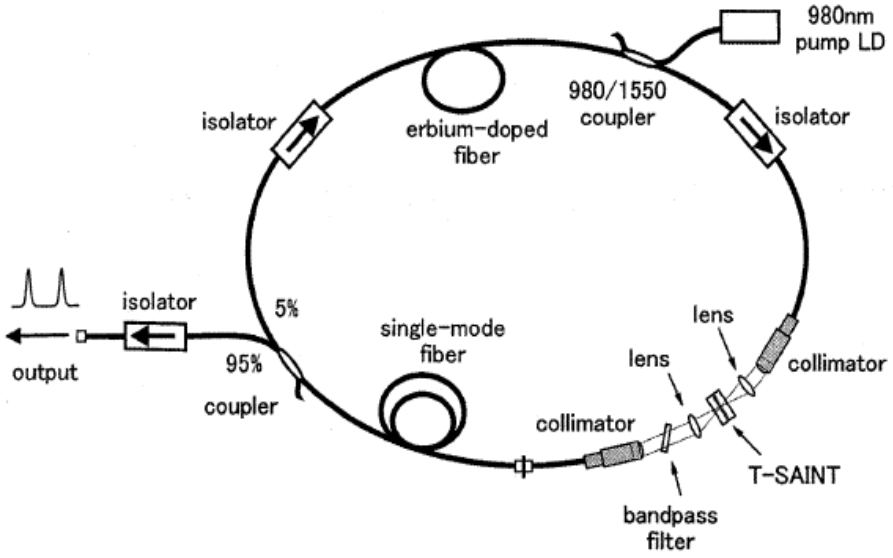

Fig. 2.11 Typical fiber ring laser incorporating CNT's [5].

The ring configuration provides the feedback mechanism for the laser oscillator. The gain of the laser is provided by an erbium doped fiber (EDF) amplifier. The layer of SWNT's has been sandwiched between two quartz slides which have been covered with an anti-reflective coating. The light is coupled into the SWNT's using an aspherical lens. A matching aspherical lens couples the transmitted light back into the fiber cavity. The laser is designed to operate at telecom frequencies. The output

spectrum is shown in figure 2.12.

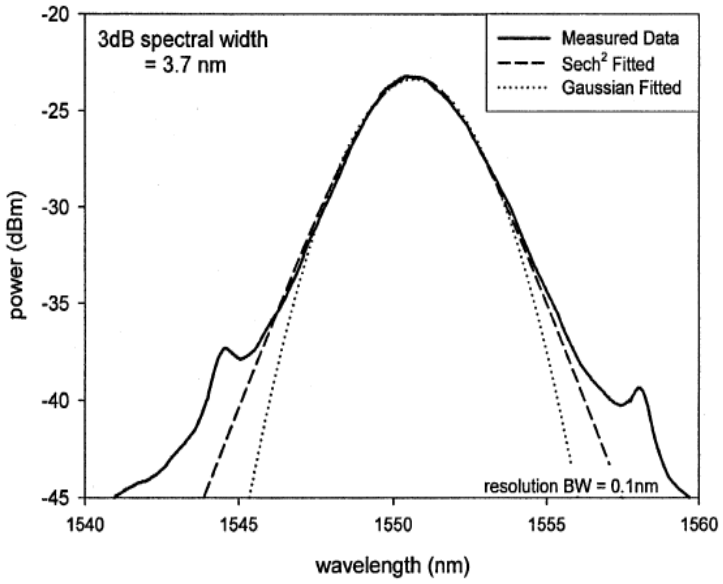

Fig. 2.12 Typical output spectrum of a fiber ring laser [5].

The spectrum was measured to be 3.7 nm at 3 dB from its peak and have a $sech^2$ profile. The pulse widths were measured to be 1.1 ps at full width half maximum (FWHM), giving a time bandwidth product of .52.

Since then, many ultrashort fiber lasers have been built that can achieve pulsewidths on the order of a 100's of femtoseconds. Figure 2.13 shows the output pulse autocorrelation trace and spectrum of a fiber ring laser using a SWNT-polyvinylalcohol nanocomposite SA [9]. The absorption spectrum of the SA has been carefully controlled. The pulses were observed to have a pulse width of 178 fs.

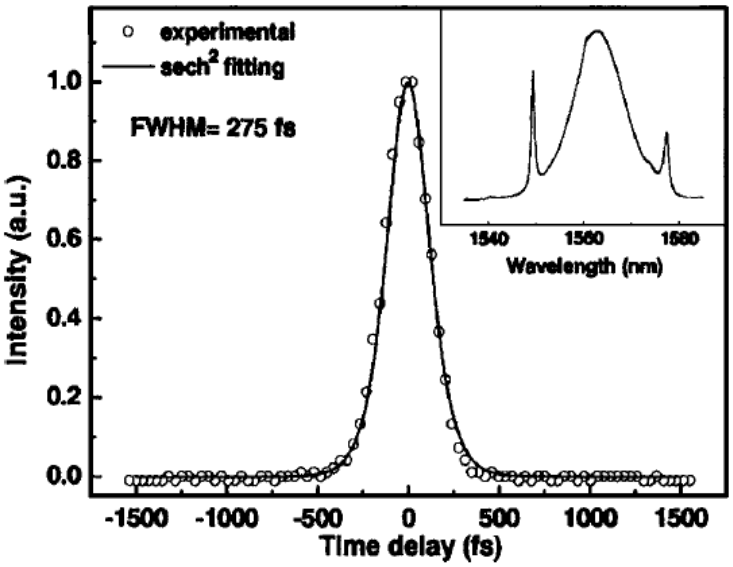

Fig. 2.13 Output spectrum and autocorrelation trace of a 178 fs MLL [9].

SAINT's have also been used in reflective cavity designs such as the one shown in figure 2.14 which uses highly reflective spherical mirrors to form a resonant cavity. A sapphire crystal doped with titanium ions, known as a Ti:Sapph, serves as a gain medium, which is optically pumped with an Argon laser [10]. The SA consists of a SWNT-carboxymethyl cellulose compound which is applied to the face of one of the mirrors. This laser also serves to demonstrate the use of SAINT's at non-telecom frequencies. The output spectrum is shown in figure 2.15.

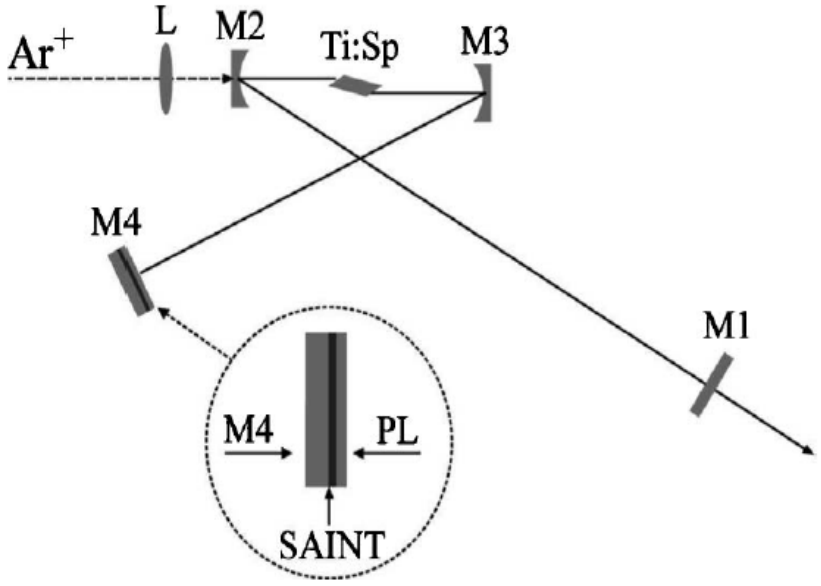

Fig. 2.14 Ti:Sapph MLL laser incorporating CNT's [10].

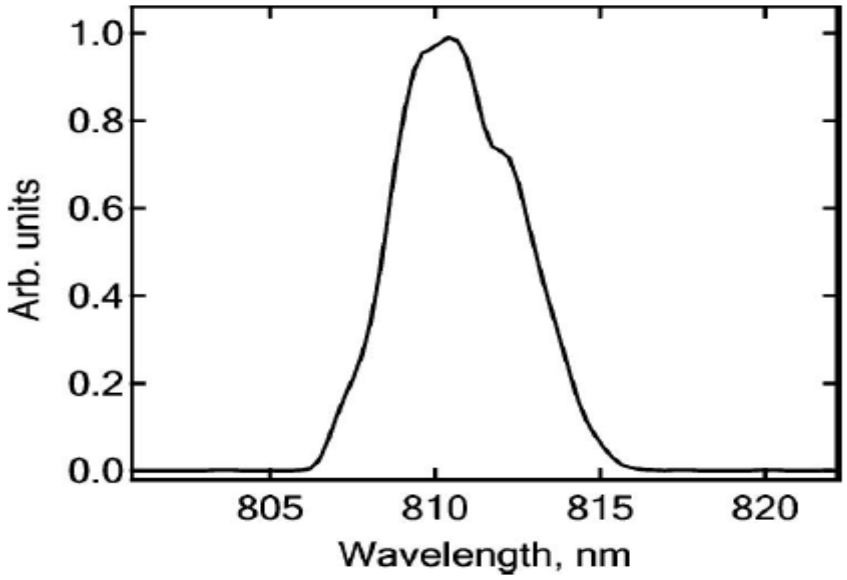

Fig. 2.15 Ti:Sapph MLL laser spectrum [10].

To date there have been many MLL's built incorporating CNT's. Table 2.1 shows a select few which highlight peak performances obtained.

Laser Type	Operating Wavelength	Pulse Width	Repetition Rate	Average Power
Er:glass [31]	1570 nm	68 fs	85 MHz	1.2 mW
SOA [32]	1571 nm	14 ps	17.2 GHz	63 mW
EDF [33]	1555 nm	464 fs	24.5 MHz	1.6 W
Yb:KLuW [34]	1046 nm	115 fs	88 MHz	53 mW
Ti:Sapph [10]	810 nm	600 fs	110 MHz	45 mW
TmDF [35]	1930 nm	712 fs	37 MHz	3.4 mW
EDF [36]	1518 to 1558 nm	2.4 ps	15 MHz	.36 mW

Table 2.1 Select CNT MLL's performance parameters

The shortest pulse width obtained so far is 68 fs using Erbium doped glass as a gain medium. The short length of a semiconductor optical amplifier was used to build a 17.2 GHz rep rate laser, while and EDFA was used to generate 1.6 Watts of average power. SWNT based MLL's have been made at various wavelengths including around 1 and 2 μm and spanning the C, 1530 to 1565 nm, and L, 1565 to 1625 nm, bands of the optical communication window. MLL's in the very NIR have also been demonstrated. Tuneable laser sources have been developed, including an EDF pumped MLL's tuneable over 40 nm [36].

As was previously mentioned, graphene has also been used to mode-lock lasers [37]. To date, there have been few reports of graphene based MLL's as the field is very new, the first being in 2009 [4].

Chapter 3

Experiments Involving Carbon Nanotubes

Chapter 3 deals with the implementation of a fiber ring laser incorporating CNT's as the SA. Section 3.1 discusses the CNT samples used. Section 3.2 details the measurements of both the linear absorption spectrum and nonlinear absorption characteristic of the samples. Section 3.3 gives an overview of the particular ring laser configuration and the method by which the output was characterized. Section 3.4 discusses the laser transition from CW to pulsed operation. Section 3.5 provides an analysis of the laser in the frequency domain, leading to the conclusion that the laser is a soliton source. The characteristic aspects of a soliton laser are described and explained. Section 3.6 discusses the laser output in both the time and frequency domains at various pumping powers. The laser is found to harmonically mode-lock at high intracavity powers. Section 3.7 discusses what happened to the SA laser after the SA had been damaged due to high intracavity power.

3.1 Description and source of the samples

The CNT based SA's were generously provided by Li Wei at Wilfrid Laurier University. The CNT's were deposited onto the face of a standard APC (angle polished connector) fiber. The deposition method consisted of mixing 10 ml of ethanol and .5 mg of CNT's in a sonic bath for 10-20 minutes, then dipping the connector face into the solution while being pumped with a 980 nm laser [38]. The CNT's are attracted to the face via thermophoresis [39]. When the connector faces are aligned, the CNT's form a thin film through which light is conveniently coupled into and collected out of, figure 3.1. The patch cords are inserted into a mating sleeve and firmly secured. This design creates an optical module which is easily integrated into conventional fiber optic systems. From now on, I will call this module the CNT device.

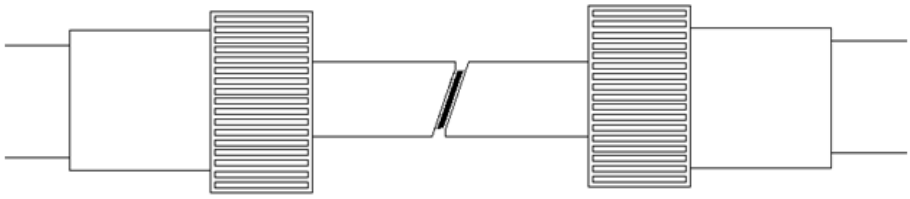

Fig. 3.1 CNT device.

3.2 Carbon Nanotube Characterization

3.2.1 Linear Measurements

First, a linear absorption spectrum of the samples was made, which included both the S-band and the C-band from 1460 nm to 1570 nm where our EDFA gain spectrum lies. The linear absorption of both samples were measured using an external cavity

laser (ECL) tuneable source. A low power signal of 0 dBm was sent through each sample and the transmission was compared with the laser output. The wavelength was incremented in 1 nm steps. The results are shown in figure 3.2.

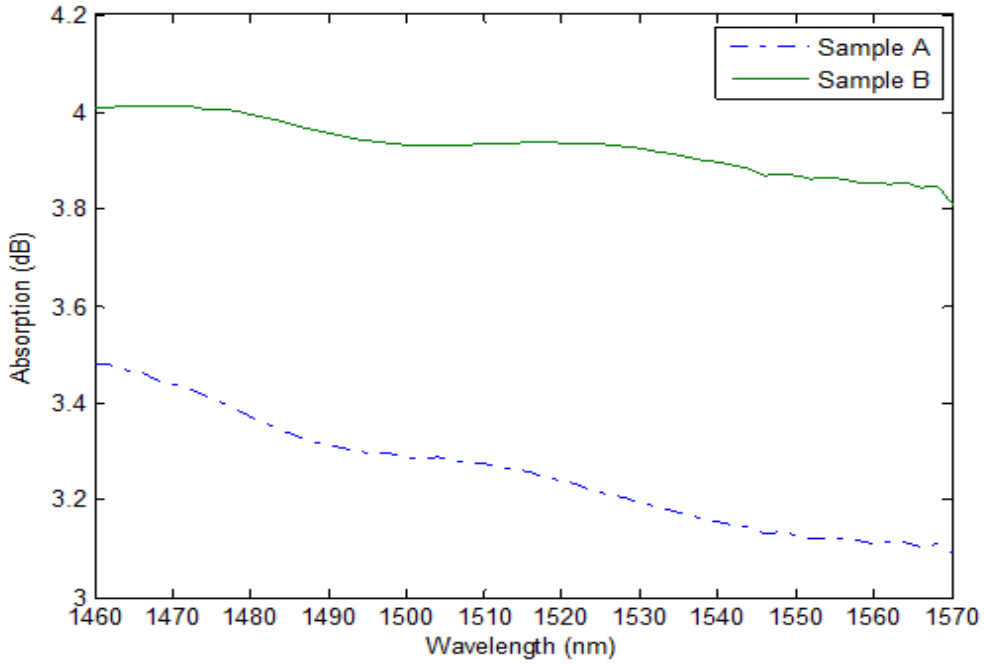

Fig. 3.2 Linear absorption of CNT devices.

Both samples show some wavelength dependence of the absorption spectrum. Sample A shows a lower level of linear absorption than B across all wavelengths measured.

3.2.2 Nonlinear Measurements

To better understand the nonlinear absorption of our samples, we proceeded to make a measurement to quantify the variables in equation 2.6. Towards this goal, a pulsed signal was sent though the CNT devices at various power levels, and the absorption in the device was measured as a function of input intensity. A pulsed source was used

in order to minimize any thermal effects that may be present and to avoid damage at high input powers. The nonlinear absorption characteristics of the CNT's were measured using the setup shown in figure 3.3.

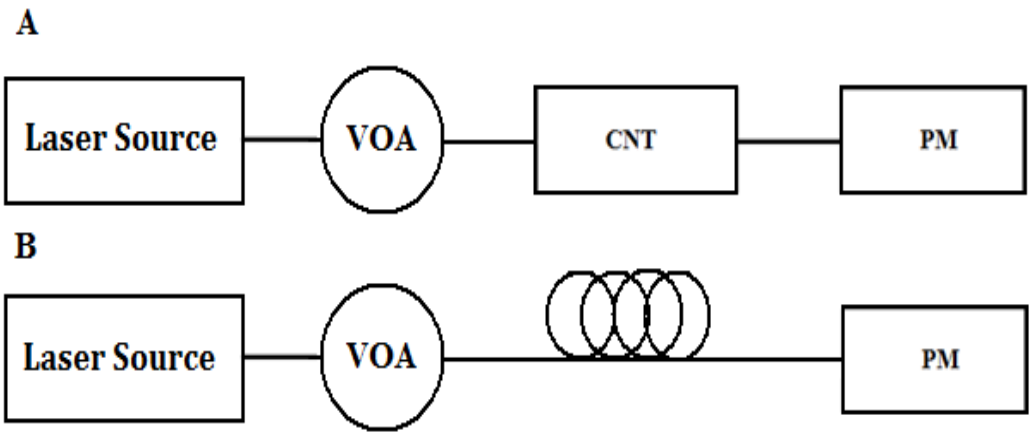

Fig. 3.3 Two measurement made to determine nonlinear absorption.

The pulsed laser source was connected to the high power variable optical attenuator (VOA). The attenuator was used to control the power hitting the nanotubes and the transmitted power was recorded (A). The measurement was made by starting with an attenuation of 50 dB on the VOA and in steps decreasing this attenuation to 0. A second measurement was then made on a length of SMF of equal length to that of the CNT device (B). The VOA attenuation was increased beyond 50 dB, such that the total attenuation of the VOA at 50 dB and CNT in the first measurement and VOA alone in the second were equal. This was done in order to simulate the unsaturated absorption of the nanotubes. In this way, the first transmission data point of each measurement would be equal. The attenuation was then stepped down in an identical way to the first run. The measurement made without the CNT was then subtracted from the measurement made with it to give the nonlinear change in transmission.

The laser source was characterized to determine the peak power of the pulses that would strike the nanotubes. The pulses were sent through the high power VOA and then through a length of SMF-28 fiber equal in length to that of the input pigtail on the CNT device before being measured. This was done to account for any pulse broadening effects that would be present in the experimental components prior to hitting the CNT's. The pulse widths were measure using a Femtochrome autocorrelator, and were found to be 800 fs. The average power was measured to be 3.5 dBm. At 20 MHz this gives a peak power of around 150 W. The mode field diameter (MFD) of Corning SMF-28 is 10.4 μm at 1550 nm [40]. This leads to a peak optical intensity of 42.5 $^{MW}/_{cm^2}$.

The normalized change in absorption of the CNT's was calculated by subtracting the change in transmission from 1, and converting it to a linear scale, it is shown in figure 3.4.

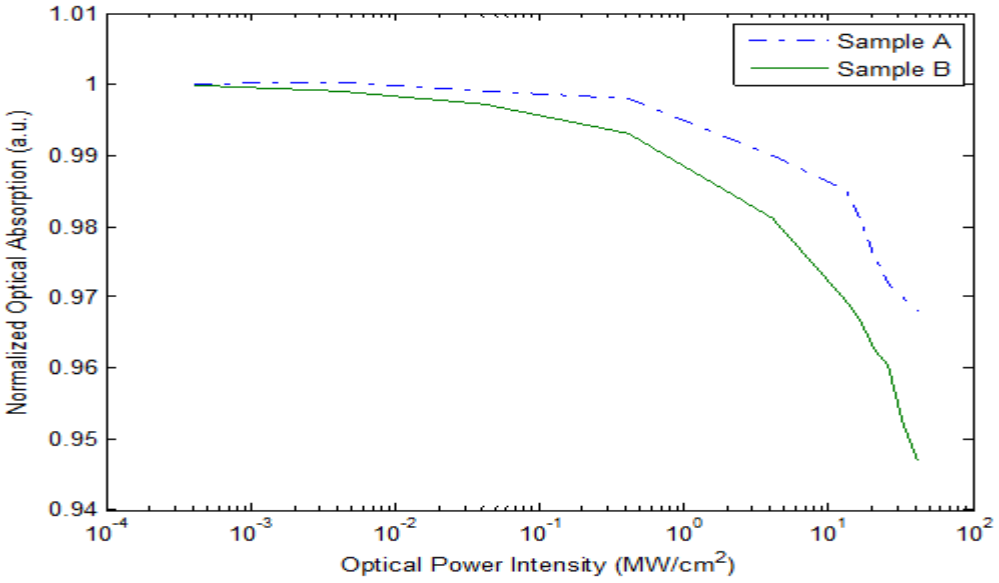

Fig. 3.4 Normalized absorption vs intensity of CNT devices.

Sample B shows a steeper and more pronounced nonlinear absorption. At maximum intensity, the change in absorption is slightly greater than 5%. Sample A has a maximum change in absorption of slightly greater the 3%. Neither absorber appears to be at its maximum saturation which would be indicated by a leveling off of the absorption curve. As a consequence we are not able to completely determine the nonlinear characteristic modeled by equations 2.3 and 2.6. as the non-saturable absorption b_0 remains unknown. We can express the logarithmic absorption vs intensity curve as

$$T_t = exp[-[b_0 + \frac{s_0}{(1 + I/I_{sat})}] \tag{3.1}$$

where T_t is the change in transmission. We can calculate the SAM coefficient, which is simply the slope of the linear curve. The SAM for sample B was 5 percent over 40 $\frac{MW}{cm^2}$, while for A it was 3 percent over 40 $\frac{MW}{cm^2}$.

3.3 Fiber ring laser

One of the goals of this thesis was to characterize a passively MLL incorporating CNT's. The CNT devices were used as the mode-locking element in a fiber ring laser, figure 3.5, similar to the one shown in figure 2.11.

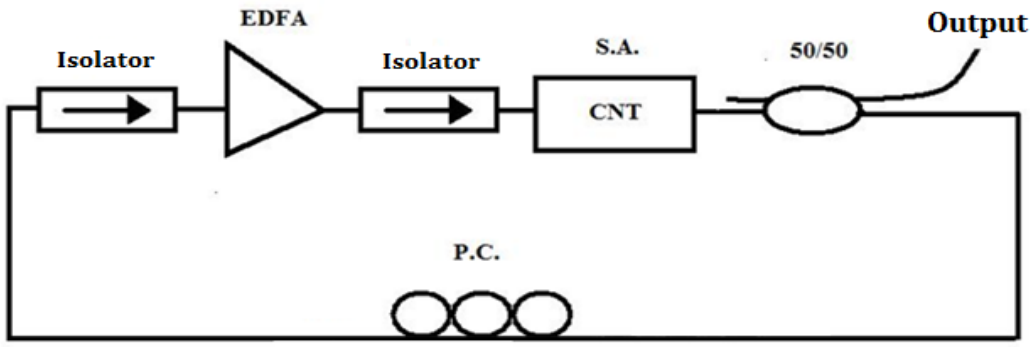

Fig. 3.5 Fiber ring laser.

The fiber ring laser consists of an EDFA as the active gain element, unless otherwise stated a Pritel FA-18 is used, two isolators to ensure unidirectional operation and to suppress reflections, a polarization controller (PC) provides an intracavity mechanism to adjust for polarization dependent loss, and a 50/50 coupler to couple the signal out of the cavity. This design is typical of fiber ring lasers incorporating CNT's [5]. The total cavity length was on the order of 20 m. The cavity output was measured by splitting the output signal using another 50/50 coupler, sending one branch to an Agilent 86142B optical spectrum analyser and the other to a 10 GHz photodiode connected to a 100 MHz oscilloscope, figure 3.6. In the time domain, this measurement system is limited by the oscilloscope, which has a rise time of 3.5 ns. Any signals detected with pulsewidths on the order of the rise time or shorter will generate the oscilliscope's impulse response.

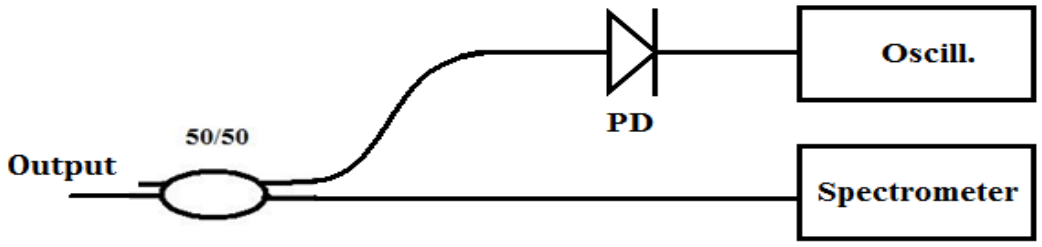

Fig. 3.6 Fiber laser output.

3.4 Mode-Locking of the Laser

The EDFA was turned on and the pump current was slowly increased until the cavity began to lase, figure 3.7. The polarization controller was then adjusted to maximize the spectral peak. At a pump current of 40 mA, the laser became mode-locked. The MLL spectrum is shown in figure 3.8.

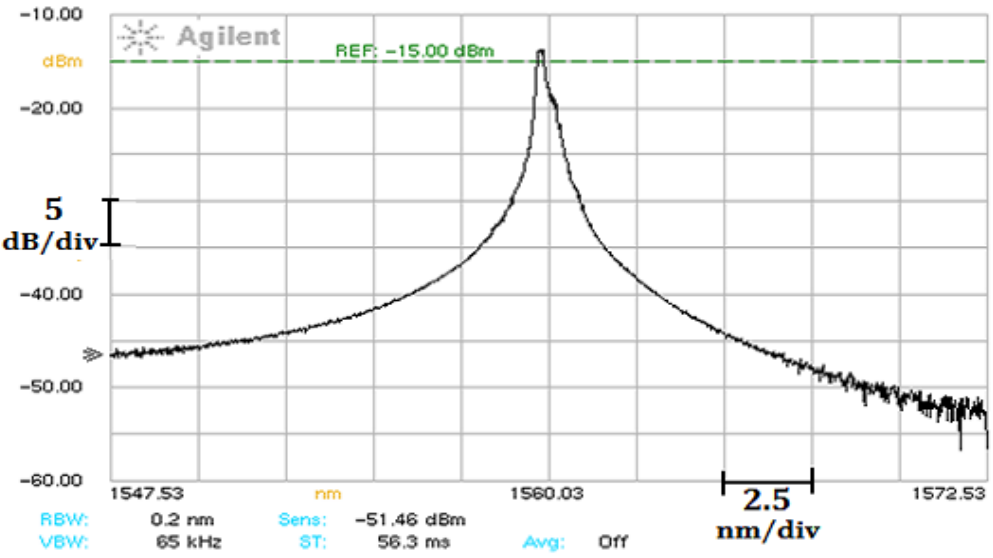

Fig. 3.7 Cavity lasing at a pump current below that required for mode-locking.

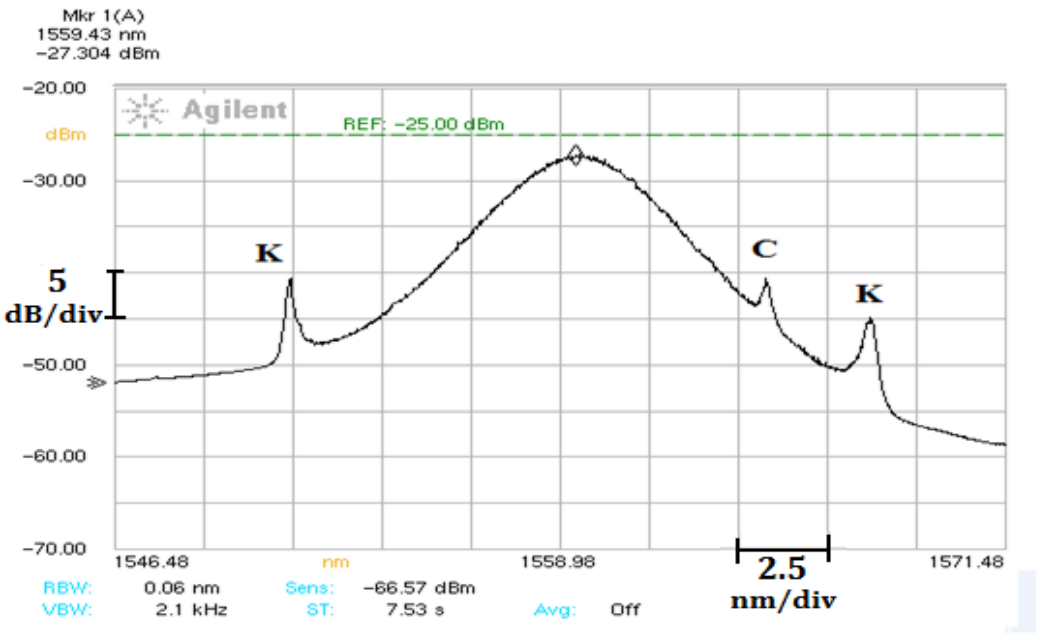

Fig. 3.8 Spectral content of the fiber ring laser at 40 mA of pump current.

There was a noted performance difference in the two CNT samples. Sample B operated in a 'turn key' manner, meaning that once setup, the pulsing of the cavity could be switched on and off simply by adjusting the pump current. It was relatively robust against changes to the orientation of the polarization controller paddles. Fiber ring lasers made using sample A were more difficult to operate, showed strong polarization sensitivity, and required more intracavity power before the onset of mode-locking. This is assumed to be due to its weaker nonlinear response as illustrated in figure 3.4. As a result, all of the following experiments were done using the B sample.

3.5 Solitons

The spectrum of the laser shows the characteristic signs of a soliton laser source. In 1973 Hasegawa and Tappert [41] predicted the existence of temporal solitons in optical fiber. In 1980, this was experimentally verified by J.P. Gordon et al [42] using a color-center laser.

To first approximation, solitons in optical fiber result from the offsetting effects of chromatic dispersion, caused by the frequency dispersion in optical fiber, and self phase modulation (SPM) caused by the nonlinear Kerr effect. These effects can be modeled using the nonlinear Schrödinger (NLS) equation, equation 3.2 [43]

$$iL_D\frac{du}{dz} - \frac{s}{2}\frac{d^2u}{dt^2} + \frac{L_D}{L_{NL}}p(z)|u|^2u = 0 \tag{3.2}$$

where z represents propagation along the axis of the fiber, u is the normalized electric field envelope, s is the sign of the second order dispersion β_2, $p(z)$ governs power variations of the signal along the fiber, L_D is related to the chromatic dispersion and L_{NL} is related to the fiber nonlinearity. The first two terms represent the linear dispersion while the third term represents the Kerr nonlinearity. In a medium with negative second order dispersion such as anomalous SMF, this equation predicts that a pulse can travel without changing its temporal profile as long as the total loss is zero. In a fiber ring laser, this condition can be satisfied when the gain provided by the EDFA offsets the losses in the fiber and the output coupler. The solitonic solution to equation 3.2 takes on a *sech* profile [43].

Solitons have been extensively studied in many fields [44, 45] and are of particular use in telecommunications due to their ability to maintain a constant pulse profile over

long propagation distances. Soliton lasers are robust and will maintain a constant output even when subjected to a weak perturbation [46].

3.5.1 Soliton Sidebands - Kelly Sidebands

The spectrum in figure 3.8 has a number of sharp peaks, labelled K and C, that are not accounted for in equation 3.2. The peaks labelled K are a feature referred to as soliton sidebands or Kelly sidebands. They are a spectral feature seen in soliton fiber lasers, particularly as the pulse width approaches the femtosecond regime. They are named after S. M. J. Kelly who first explained their origin in 1992 [47]. To understand the Kelly sidebands, we have to consider that the soliton pulse travelling around the loop in the fiber ring experiences a periodic perturbation as it travels through the high gain and highly nonlinear EFDA followed by the higher dispersion and lossy SMF and then back into the EDFA. The pulse will expand and contract in the time domain, known as breathing, and will emit non-solitonic radiation in the form of a dispersive wave in an attempt to readjust itself to the steady state. This results in a resonant energy transfer between the soliton and those dispersive waves whose phase is matched to that of the soliton and when the round trip phase delay of the radiation emitted is an integer multiple of 2π [48]. Broader spectrum pulses will have a higher energy transfer rate, which suggests that sideband formation may be the ultimate limiter of short pulse generation in fiber soliton lasers [49].

The sidebands will appear symmetrically around the soliton carrier frequency and many sidebands can appear. The frequency separation between the soliton carrier and the Kelly sidebands is given in equation 3.3 [3]

$$\delta\nu_n = \pm\frac{1}{2\pi\tau_p}\sqrt{1+8n(z_0/z_a)} \tag{3.3}$$

where τ=2ln(1+$\sqrt{2}$)τ_p is the pulse FWHM, z_0 is the soliton period, z_a is the amplifier period and n is an integer.

Using a FWHM of 1 ps, which will be justified in the next section, and a soliton period over amplifier period of 1.33, which is approximate as the length of the amplifier is unknown but can be inferred from the laser repetition rate, the calculated wavelength separation between carrier and sideband was 7.76 nm, whereas it was measured to be 7.9 nm. Given the approximation of the amplifier period, the theoretically derived wavelength spacing is in good agreement with the measured value.

3.5.2 Soliton Sidebands - Polarization Locked Vector Soliton

The third peak, labelled C, in figure 3.8 arises as a result of polarization mode dispersion (PMD) present in the fiber. It was observed that the location of the C peaks could be shifted up and down the wings of the spectrum by adjusting the polarization controller. The peaks could be brought almost to the carrier frequency and could be made to disappear by overlapping them with the Kelly sidebands.

If all fiber were completely isotropic, orthogonally polarized modes would be degenerate and SMF would truly be single mode. However, imperfections in the fiber, due to fabrication processes, bending etc leads to fiber birefringence and so orthogonally polarized modes have different propagation constants. We might expect that the difference in group velocities would prevent the formation of solitons with energies in both orthogonal modes; however, solitons are able to compensate for the linear birefringence with no-linear birefringence that arises from a combination of self and cross

phase modulation. The pulse can be modeled using the set of coupled NLS equations in equation 3.4 and 3.5 [50]:

$$i\frac{du}{dz} + i\delta\frac{du}{dt} + \gamma u + \frac{1}{2}\frac{d^2u}{dt^2} + (|u|^2 + A|v|^2)u + Bv^2u^* = 0 \tag{3.4}$$

$$i\frac{d\nu}{dz} - i\delta\frac{d\nu}{dt} - \gamma u + \frac{1}{2}\frac{d^2\nu}{dt^2} + (|\nu|^2 + A|u|^2)\nu + Bu^2\nu^* = 0 \tag{3.5}$$

where A and B are the cross phase modulation and energy exchange coefficients, respectively, u and v are the electric field envelopes along the fast and slow axes, z and t are the time and distance parameters and δ and γ are the group and phase velocity differences.

These equations have two linearly polarized soliton solutions

$$u(t,z) = u_0 sech(t - \delta z)exp(i\gamma z)\ and\ v(t,z) = 0 \tag{3.6}$$

$$u(t,z) = 0\ and\ v(t,z) = v_0 sech(t + \delta z)exp(i\gamma z) \tag{3.7}$$

The cross phase modulation causes the group velocity of one polarization to increase and the other to decrease and so travels as a non dispersive vector locked soliton [51, 52]. This periodic perturbation of the pulse leads to the creation of dispersive waves that are dependent on the state and magnitude of polarization in the fiber ring. In figure 3.9 which is the spectrum of a more strongly pumped laser, we can clearly see the four Kelly sidebands and four polarization locked vector soliton (PLVS) sidebands on either side of the carrier frequency.

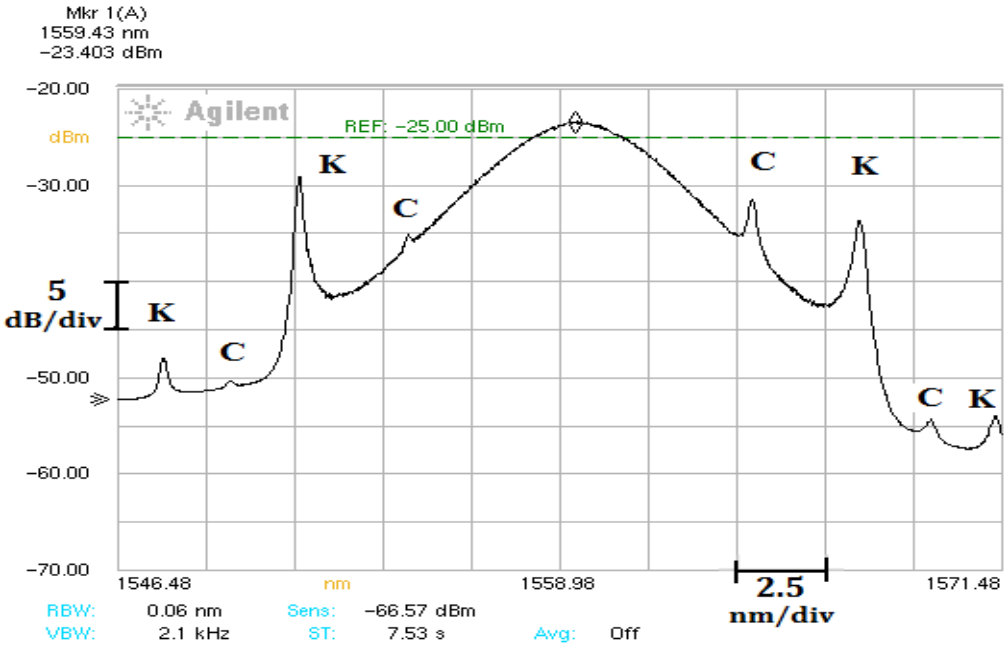

Fig. 3.9 Soliton laser spectrum with a pump current of 56 mA.

The general shape of the spectrum and the distinctive sideband features indicate strongly that this is a short pulse duration soliton.

Finally, if we take a look at a more broadband spectrum, figure 3.10, we can see that the output power of the laser is highly concentrated in the soliton and soliton sidebands, and very little power is being emitted as amplified stimulated emission (ASE) from the EDFA.

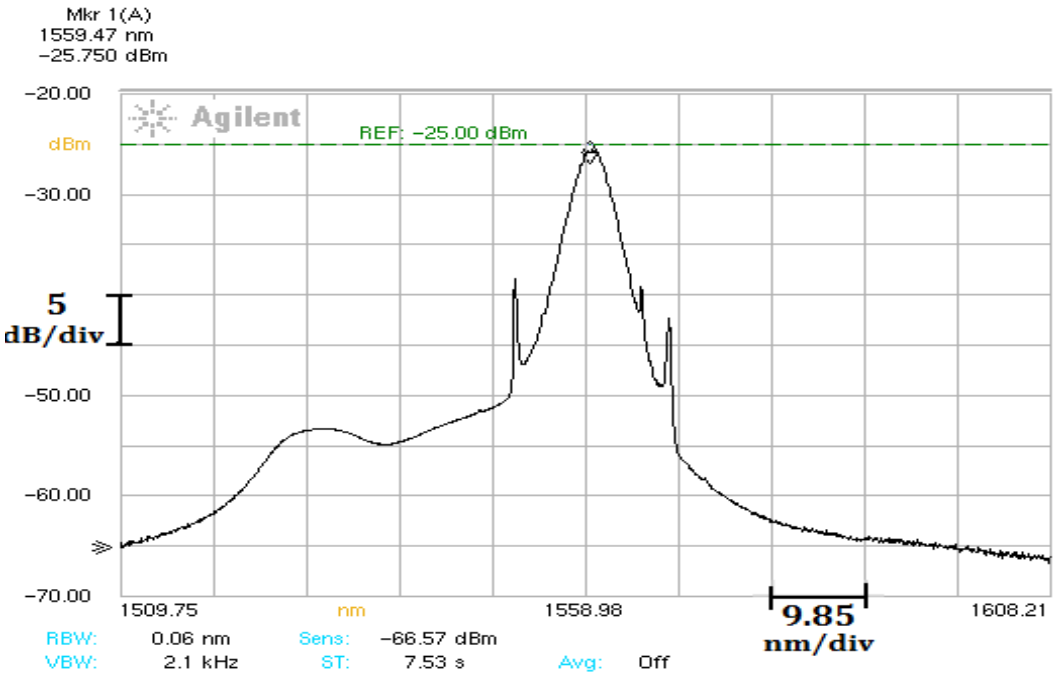

Fig. 3.10 Broadband spectrum of the laser with a pump current of 40 mA.

3.6 Analysis of the MLL

3.6.1 Spectral Domain

The spectrum of the pulse at the mode-locking threshold, at a pump current of 40 mA, was fitted to both a $sech^2$ profile and a Gaussian profile in both the linear and logarithmic power scales. This is shown in figures 3.11 and 3.12.

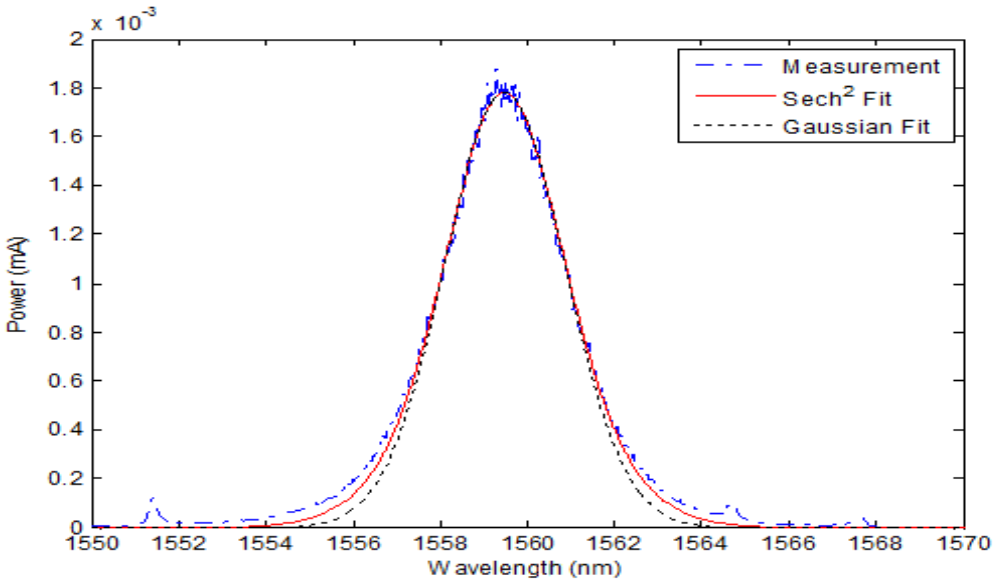

Fig. 3.11 Linear power spectrum overlaid with both a Gaussian and $Sech^2$ fit.

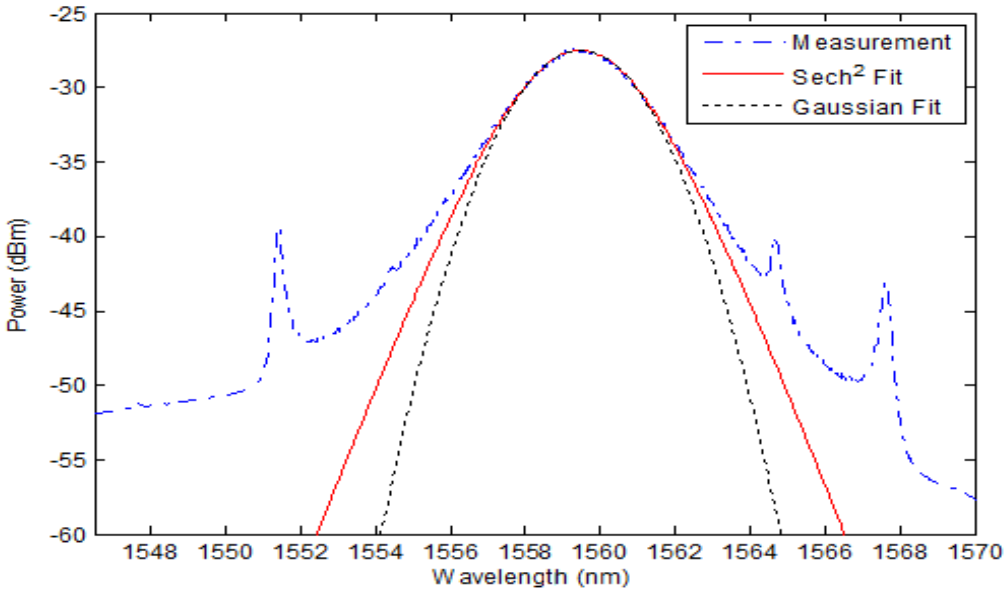

Fig. 3.12 Logarithmic power spectrum overlaid with both a Gaussian and $Sech^2$ fit.

The 3 dB bandwidth was found to be 3.34 nm. The central wavelength was 1559.5 nm. Both fits are accurate down to about 6 dB from peak power, at which point they begin to diverge. The fitting is complicated by the sidebands and the ASE pedestal, as a result neither fit accurately portrays the signal in the wings at lower power levels, however the $Sech^2$ profile seems to be a closer fit.

3.6.2 Time Domain

We now turn our attention to the laser in the time domain. Figure 3.13 shows a 250 ns oscilloscope trace.

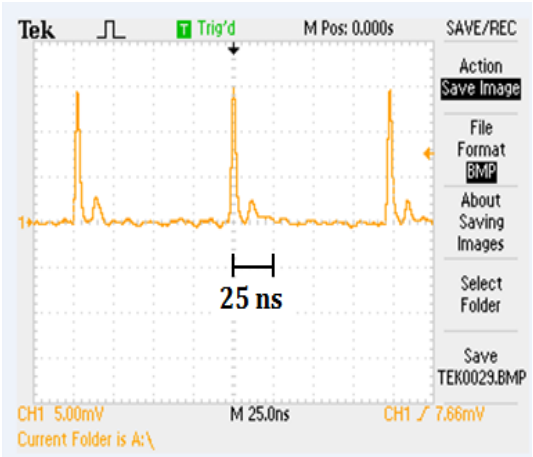

Fig. 3.13 Oscilloscope trace of the laser with a pump current of 40 mA.

From this trace we can determine the bit window to be approximately 100 ns and the repetition rate of the laser to be 9.99 MHz. The fundamental rep rate of the laser is determined by the time it takes a pulse to travel the length of the cavity, which is roughly 20 m, corresponding to a rep rate of 10 MHz. This correlates well with the observed value.

The pulsewidths cannot be measured directly using the 100 MHz oscilloscope due to the limited response time. The pulses were measured using the Femtochrome autocorrelator. The autocorrelator measurements are shown in figures 3.14 and 3.15, in linear and logarithmic power scales, overlayed with both Gaussian and $Sech^2$ fits. The autocorrelation measurements are converted to time values using a conversion factor of 1 ms equals 31 ps in real time.

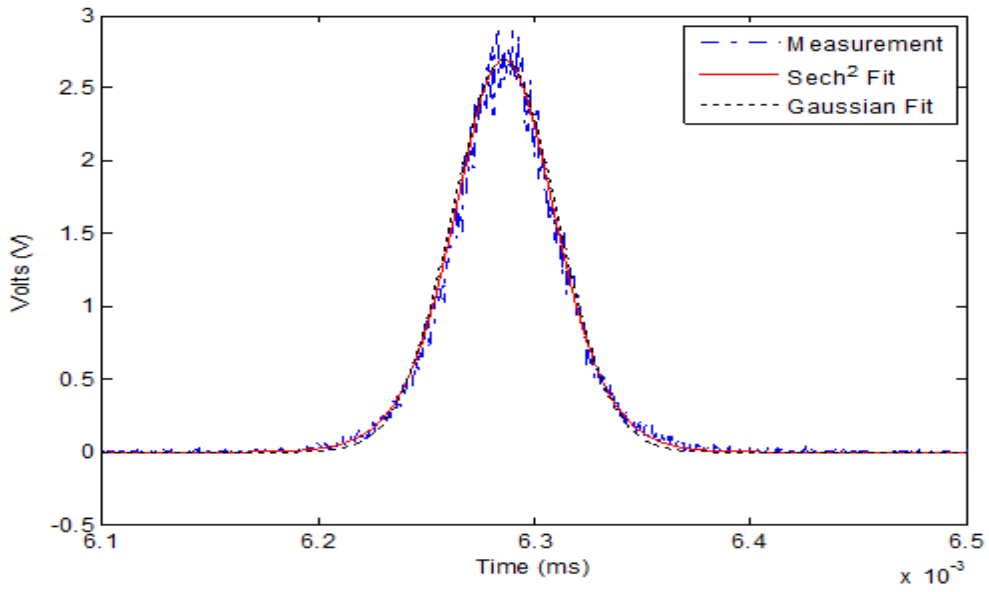

Fig. 3.14 Autocorrelation trace in a linear scale.

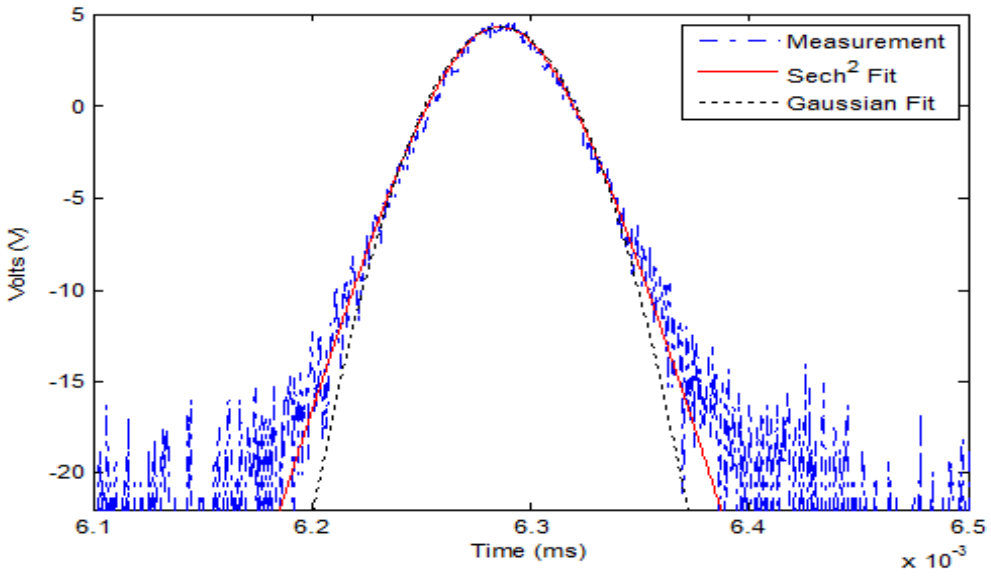

Fig. 3.15 Autocorrelation trace in a logarithmic scale.

The pulse shape fits very well to a convoluted $Sech^2$ profile, however the noise in the measurement at the edges complicates the fit. A Gaussian pulse shape cannot be ruled out.

The FWHM of the pulse was determined to be 1.09 ps in the case of a $Sech^2$ profile and 1.18 ps in the case of a Gaussian profile. The time-bandwidth product was calculated to be .441 in the case of a $Sech^2$, and .477 in the case of a Gaussian pulse.

Although the time-bandwidth product for a Gaussian pulse is much closer to the transform limited case of .44, the pulse in both the spectral domain and the time domain is more consistent with a $Sech^2$ pulse shape. It is likely that the pulse has a frequency chirp which, in combination with the dispersion in the output fiber, leads to a pulse that is not transform limited at the point at which it is measured. This is

consistent with the time-bandwidth product we see in the $Sech^2$ case.

3.6.3 Laser hysteresis

As was previously stated, the threshold for mode-locked operation in the fiber ring laser was 40 mA of pump current. Before this point the laser would operate in CW. Once mode-locked, the pump could be reduced to 36 mA of current before pulsed operation stopped and the laser returned to CW operation. This characteristic is known as pump power hysteresis [53]. The pump could also be increased to 44 mA and the peak power spectral density of the spectrum would stay constant. A number of traces taken around threshold shown in figure 3.16 illustrate this point.

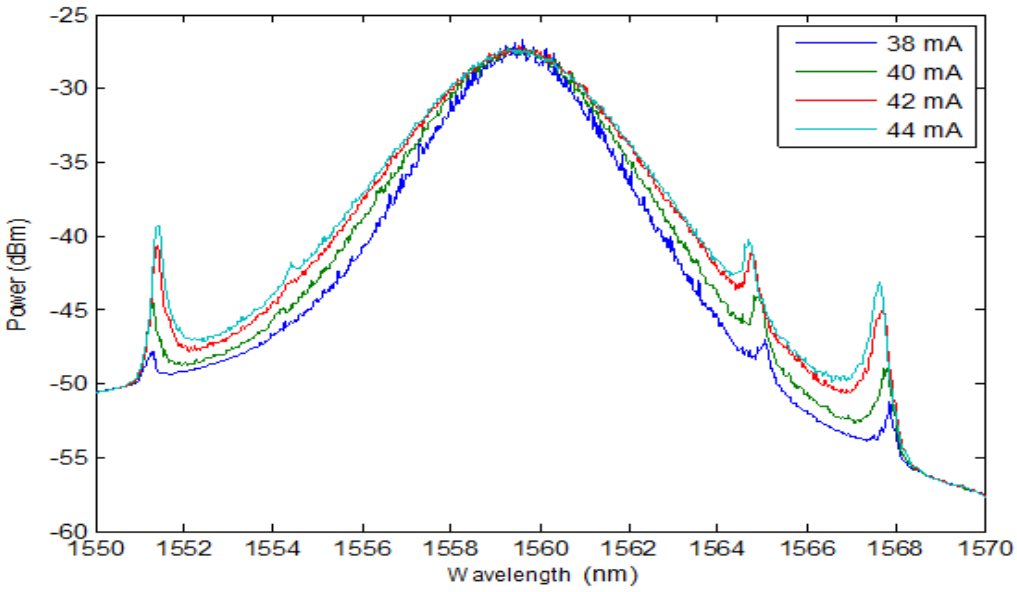

Fig. 3.16 Four spectrums around threshold pump power.

Increasing and decreasing of the pump power around threshold produces no change in the power spectral density in the peak of the spectrum of the pulse. Most of the

power injected into the cavity above the minimum power required to maintain mode-locked operation couples into the sidebands of the soliton.

Above 44 mA of pump current, the soliton jumps into another mode of operation whereby the peak power spectral density of the spectrum of the pulse locks into a higher value. Figure 3.17 shows the spectrums at nine different pump currents.

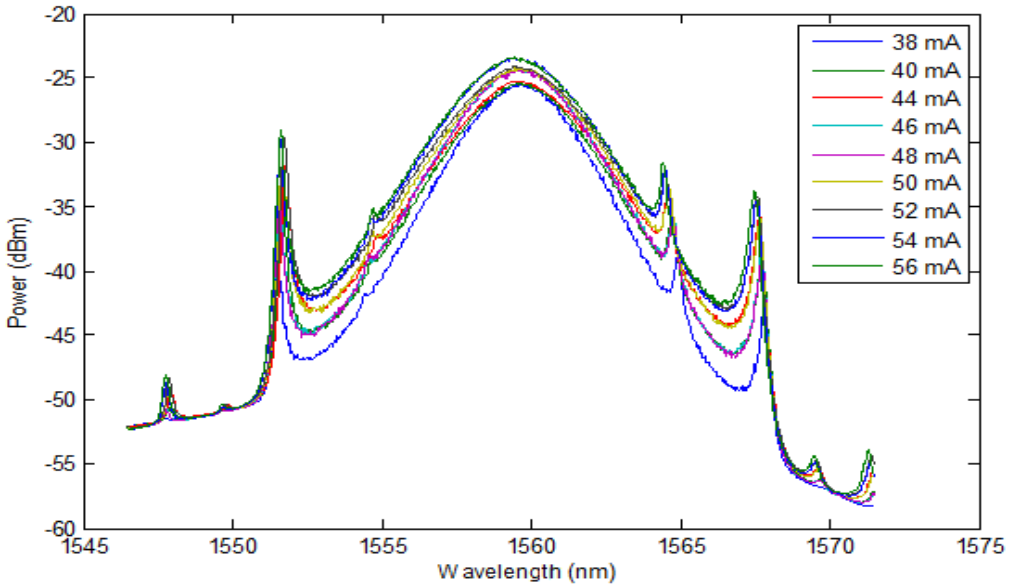

Fig. 3.17 Multiple spectrums at various pump currents.

If we take a closer look at both the peak powers, figure 3.18, and the sidebands, figure 3.19, we can see explicitly what is happening.

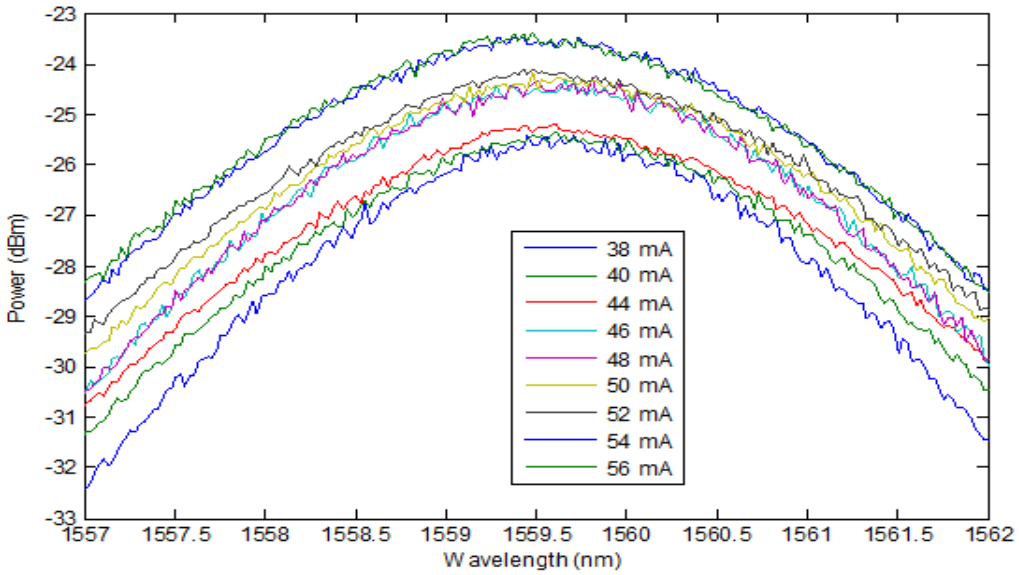

Fig. 3.18 Characteristics of the peak power spectral density at various pump currents.

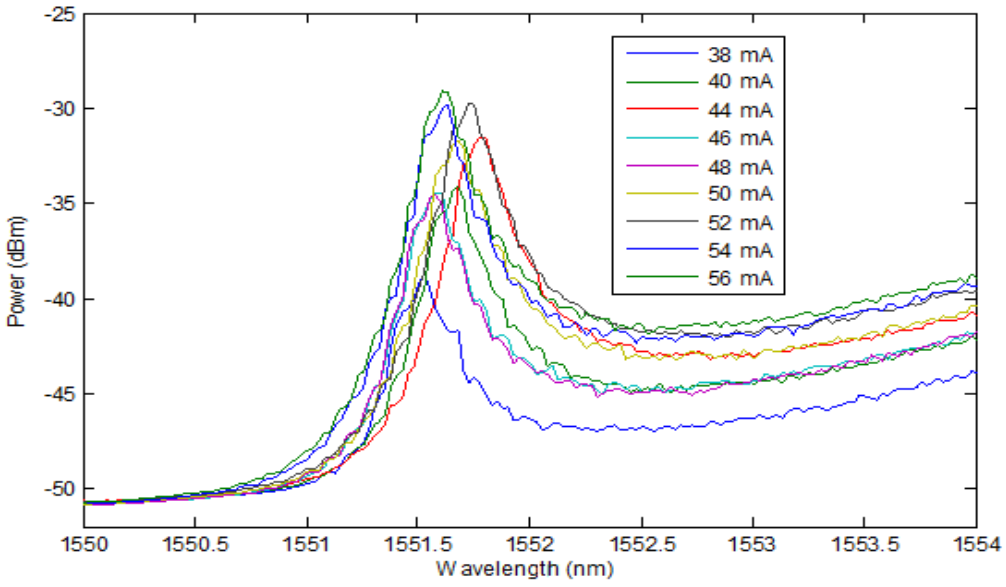

Fig. 3.19 Spectral densities of the sidebands at various pump currents.

Figure 3.18 clearly shows three levels at which the soliton spectrum locks. The separation of the levels is approximately 1 dB. We can also see that the carrier wavelength is slowly shifting towards a shorter wavelength. If we examine the sidebands as illustrated in figure 3.19, we can see that the powers associated with the peak of a locking region, red, black and dark green, are higher power then all the other intermediate values. This result shows that for a given pulse, an increase in the intracavity power corresponds to very little change in the pulse profile, but a large change in the spectral sidebands. Most of the increase in power is coupled into the non solitonic dispersive waves. This situation is described in figure 3.20

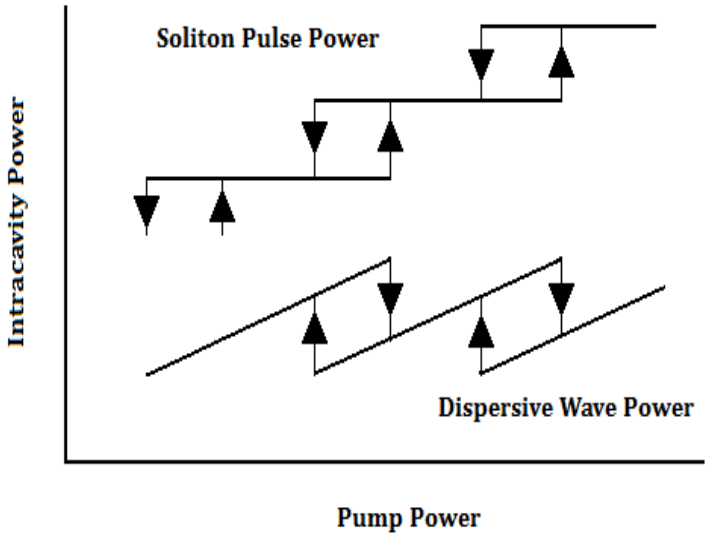

Fig. 3.20 Soliton power quantization and dispersive wave power.

This type of step function output with pump power hysteresis has been reported in soliton lasers [54].

3.6.4 Harmonic Mode-Locking

Finally, this quantized power behavior leads us to the question of where the extra power in the solitons resides, as the NLS equation supports a single solution for the given cavity dispersion and nonlinearity. To answer that question we will return to the oscilloscope output in figure 3.21

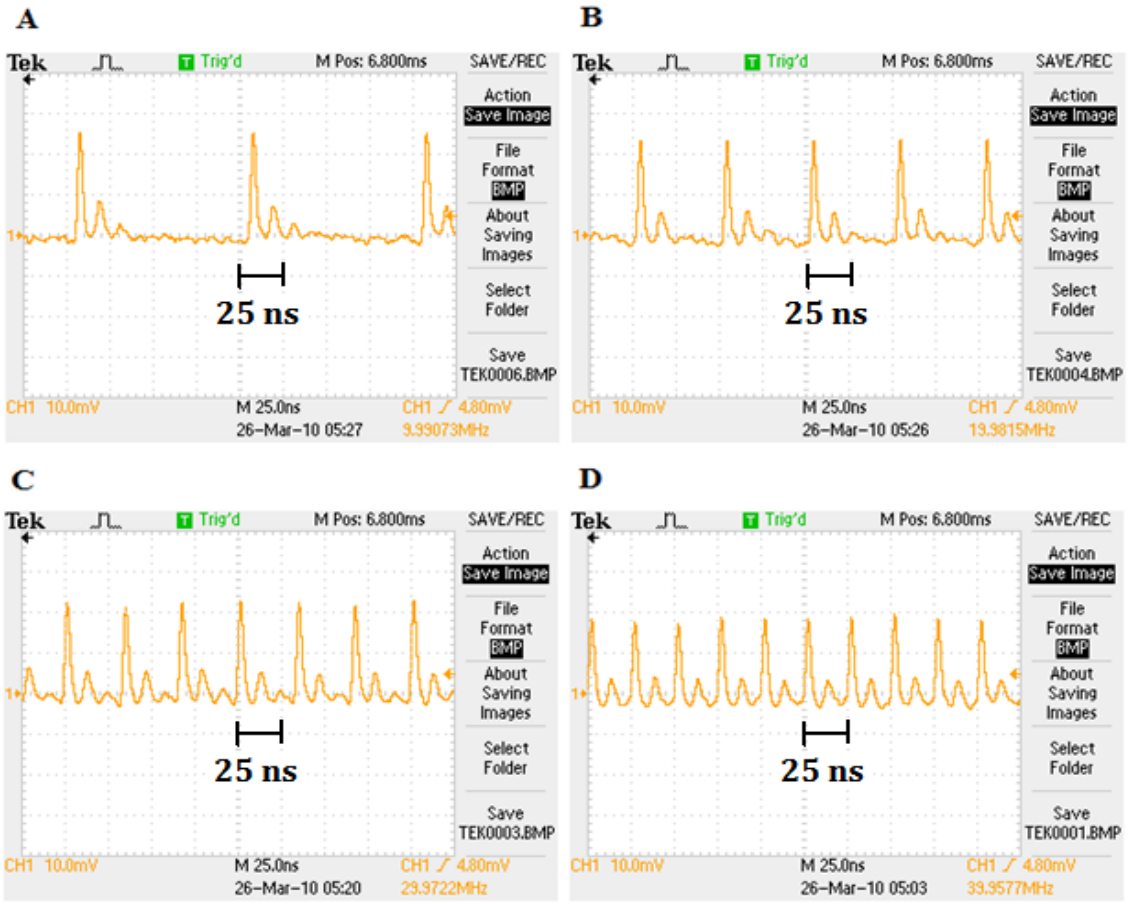

Fig. 3.21 Temporal spacing of the pulses as the pump current is varied. A, 40 mA: B, 44 mA: C, 48 mA: D, 54 mA

Figure 3.21 shows the temporal output as the pump current is increased. As the pump current is increased to the mode-locking threshold, 40 mA, we see pulses

emitted by the ring laser at the equivalent of the cavity fundamental frequency 9.99 MHz in A, which is the round trip time. The small second and third peaks trailing each pulse are a result of ringing in the oscilloscope impulse response. As the pump current is further increased, beyond 44 mA in B, the soliton splits into two solitons both circulating within the cavity and with constant spacing in the time domain. The repetition rate of the laser in figure 3.21 B is 19.98 MHz, double the frequency of the fundamental. In C and D we see a tripling and quadrupling of the fundamental cavity frequency, up to a rep rate of 39.96 MHz in the case of D as the intracavity power is increased. This phenomenon is known as harmonic mode-locking.

Harmonic mode-locking of solitons was first reported in a passive dye laser in 1988 [55] and in a SESAM laser in 1999 [56]. Harmonic mode-locked PLVS have been observed and described in 2008 [57]. Harmonic mode-locking, or multi soliton operation, has generated interest due to its ability to increase the repetition rate of ring lasers. An important characteristic of multi soliton operation is that as long as the pulses are well separated inside the laser cavity, they will have the exact same parameters, pulse width, energy and peak power, all of which are important for telecom applications.

Above a critical intracavity power, the solitons and sidebands cannot support any more energy. This can results in the pulse splitting into two or more pulses. The evolution of the pulse splitting has been described by Tang *et al.* [58].

The regular spacing of the pulses is a result of a weak force that is due to the gain depletion and recovery times in the EDFA [59]. As a soliton passes through the gain medium, it reduces the amplifiers population inversion. A subsequent pulse will effectively 'see' a lesser gain than the first. The second pulse is drawn towards the area of higher gain until both pulses experience the same gain. In effect, the pulses

exert a weak repulsive force on each other. Unfortunately, due to the weakness of this force, harmonically mode-locked soliton lasers suffer from relatively large timing jitter which is a barrier to their being used in the telecom field.

For this particular fiber ring laser the maximum achieved repetition rate was 129.8 MHz, equal to the 12th harmonic of the fundamental frequency, at an intracavity power of around 7 dBm. The harmonics seemed to be strongly dependent on the state of the polarization controller, in particular, the highest order harmonics could only be achieved under specific polarizations.

3.7 Burn Out

Unfortunately, in an attempt to achieve higher repetition rates, the lasers intracavity power level exceeded the optical damage threshold of the CNT device. An average power reading at the cavity output confirmed that as the intracavity power exceeded 6 to 7 dBm, the power output of the laser dropped over time. This change was permanent, as the cavity was tested repeatedly. An increase in the linear absorption of the CNT device indicated possible burn damage. The damage was confirmed by taking the second nonlinear absorption measurement shown in figure 3.22.

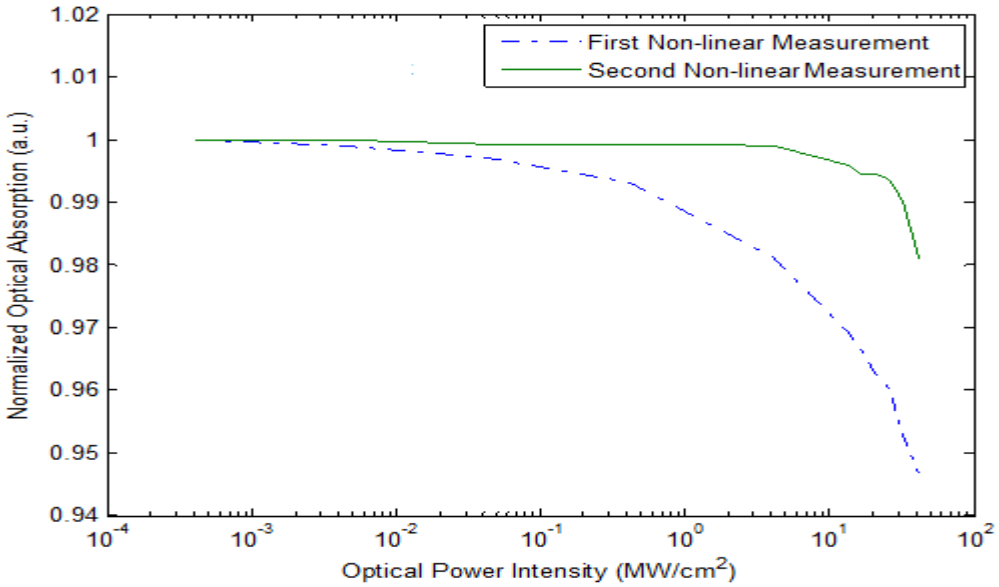

Fig. 3.22 Nonlinear absorption characteristic of CNT device before and after optical damage.

The linear absorption of this sample had also dramatically increased from less than 4 dB to over 9 dB.

3.7.1 Reduced Saturation in the Spectral Domain

Although the CNT device had been damage, it was still possible to mode-lock the fiber ring laser. The following sets of experiments were conducted using the damage CNT device.

After the CNT device had been burned the fiber laser became much harder to mode-lock. The threshold for mode-locking increased to greater than 50 mA of pump current, and the polarization controllers needed to be much more carefully aligned. Finally, there was a pronounced background CW signal circulating inside the loop along with the mode locked pulses. Three spectrums around threshold are shown in

figure 3.23.

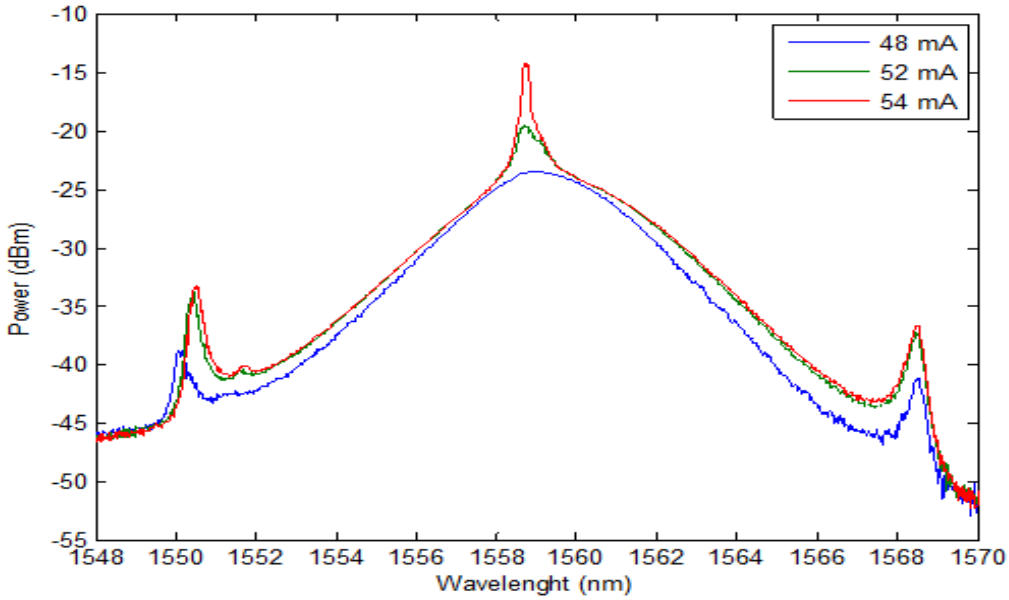

Fig. 3.23 Spectra around the threshold pumping current.

At 52 mA the fiber laser mode-locks with the CW signal clearly visible around the carrier frequency. When the pump current is reduced to 48 mA, the minimum pump current needed to preserve mode-locked operation, the CW signal is no longer visible in the spectrum. It is either completely gone or it carries so little power that it is undetectable in the pulse spectrum. At this point the Kelly sidebands of the pulse are also significantly reduced, similar to the case previous to the CNT device being damaged. If the pump current is increased to 54 mA, the spectrum is almost identical to the threshold spectrum except for an increase in the power spectral density of the CW signal. In particular, the Kelly sidebands remain the same indicating that there is no increase in the pulse power. All the additional intracavity power has coupled directly into the CW signal.

The 3 dB bandwidth of the lowest pump current spectrum was found to be 3.5 nm, and if we ignore the CW signal, the 3 dB bandwidth of the threshold pump current was 3.6 nm. We should note that the first MLL built with the undamaged CNT had consistently lower 3 dB bandwidths in the 3.3 to 3.4 nm range. The Kelly sidebands in figure 3.23 are also slightly farther from the carrier wavelength at 8.9 nm than those of figure 3.8, which were measured to be 7.9 nm from the carrier. From equation 3.3 we note that v_n is a function of t_p^{-1}, indicating that the Kelly sidebands should be further from the carrier for shorter pulse widths, which we would expect given a broader bandwidth. Autocorrelations of the pulses indicated that they were in the 800 to 900 fs range depending on whether a Gaussian or $Sech^2$ pulse profile was chosen. When the pump current was increased beyond 54 mA the laser output spectrum showed a quantized jump similar to the previous set of experiments, it is shown in figure 3.24

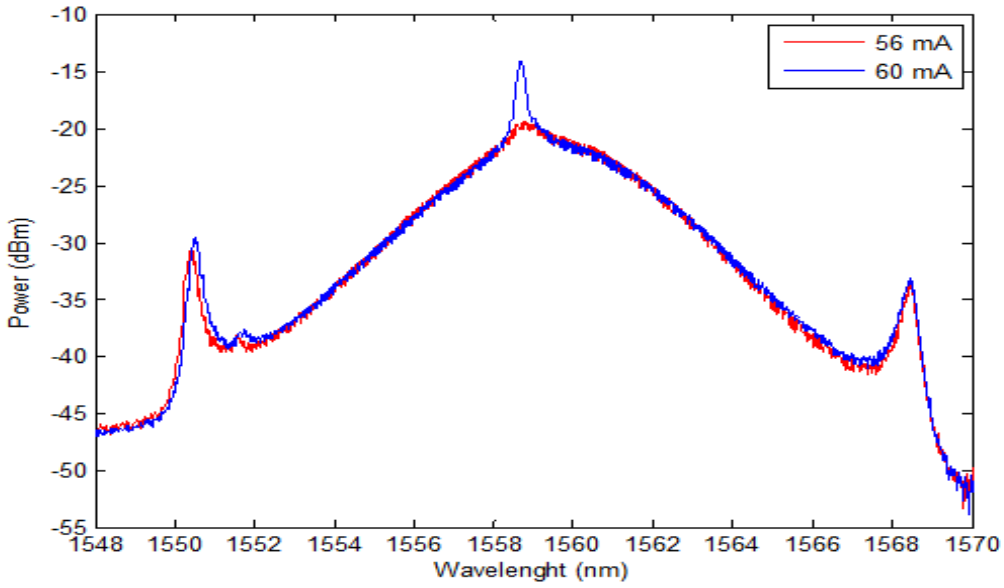

Fig. 3.24 Two Spectra in the second quantized power level.

We can see that the power spectral density has locked into a power level roughly 4 dB higher than in figure 3.23, and with a strong CW component co propagating with the pulse. As the pump power is increased or decreased, most of the energy couples into this CW signal. A feature of the spectrum is that it is not a smooth function of wavelength, but is composed of many thin, sharp peaks and valleys.

3.7.2 Reduced Saturation in the Time Domain

We now turn out attention to the time domain and look at the laser output on the oscilliscope.

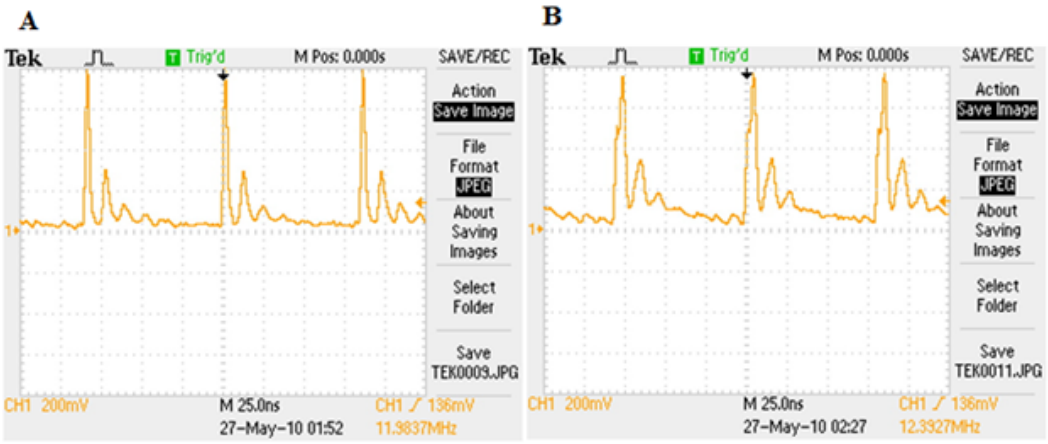

Fig. 3.25 Oscilliscope traces as the intracavity power is varied.

Figure 3.25 A shows the laser output associated with 52 mA of pump current, at threshold. The pulses are sharp and riding on a small CW signal, which can be seen by the small offset in the time domain. In B we see the output of the pulses at 56 mA. The pulses are not as sharp and it looks as though there are two pulses traveling very close to each other. We turn to the autocorrelation trace in figure 3.26

for confirmation.

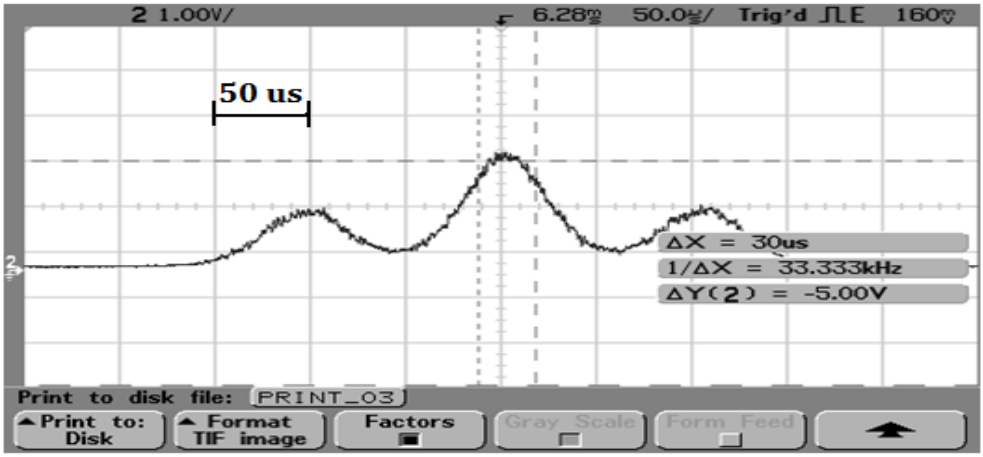

Fig. 3.26 Autocorrelation trace at 56 mA.

Figure 3.26 indicates that there are two co-propagating pulses traveling within a couple of picoseconds of each other. This indicates that the output of the laser at this power is a bound soliton.

3.7.3 Bound Soliton

It can be demonstrated that when two solitons slightly overlap, they can form a stable bound state. These can be two pulse states, multiple states and periodic arrays of pulses [60]. Solitons formed in a MLL are known to have an oscillating tale, when the tails of two or more solitons interact they can fall into fixed discreet separations. The solitons need not be of the same magnitude, however, they will have a phase difference. This fixed phase difference accounts for the non smooth spectrum, as the solitons are partially destructively interfering with each other. These two solitons can effectively be considered a single state [61].

Bound solitons are of interest in developing ultra high repetition rate lasers. Recently, a bound soliton fiber ring laser has been demonstrated with a repletion rate of 125 GHz [62].

3.8 Chapter Conclusion

A fiber ring laser incorporating CNT's was built and characterized. Several characteristic properties associated with a soliton laser source were identified, including the soliton sidebands. Initially the laser was found to operate in a 'turn key' manner, with pulse widths on the order of 1 ps with a bandwidth of 3.5 nm and a rep. rate of 9.99 MHz. The output of the laser was characterized over a range of intracavity powers, and was found to harmonically mode-lock with equal spacing between pulses at higher powers. The highest repetition rate that was reached was 129.8 MHz, 13 times the fundamental. The damage threshold was determined to be around 7 dBm. Finally, with the CNT device having a higher linear loss and lower modulation depth, the fiber ring laser was found to generate bound soliton pairs.

Chapter 4

Experiments Involving Carbon Black

As was mentioned in the background section, individual carbon black particles can be thought of layers of stacked graphene with a significant amount of disorder. With this in mind, it is theorized that they will exhibit some level of saturable absorption. Assuming that the number of layers scales with the particle size, we would expect smaller particles to exhibit a larger saturation depth in much the same way as layered graphene. Section 4.1 will provide a brief overview of the samples used. The goal of the following set of experiments was to determine if carbon black exhibits a measurable optical nonlinear response. Towards this goal an optical probe setup was designed and built to measure optical absorption as a function of intensity. The setup was designed to pass either CW or pulsed signals in the NIR, specifically at 1310 nm and 1550 nm, through a thin layer of carbon black deposited on glass and compare the absolute absorption over a large range of input intensities. These two wavelengths are important to optical networks as 1310 nm in the zero dispersion point for standard optical fiber and 1550 nm has the lowest loss. The details and results of this experiment are discussed in section 4.2. Section 4.3 details a similar set of ex-

periments conducted on carbon black in a vacuum environment. Section 4.4 discusses a novel result discover during the experimentation process for using carbon black on an optical fiber as an electron source. Section 4.5 discusses a Q-switched ring laser incorporating carbon black.

4.1 Material Description

Carbon black is a granular form of amorphous carbon generally characterized by its average particle size (APS). It is produced on an industrial scale by subjecting heavy residual oil feedstock to extremely high temperatures in an anaerobic environment. This process results in virtually pure elemental carbon in the form of colloidal particles.

It is typically used as a reinforcing agent in rubber and plastic products. Due to its large absorption bandwidth carbon black neither reflects nor transmits much incident radiation, making it ideally suited as a black pigment and as a protective coating against ultraviolet and infrared (IR) light. Due to its electrical properties, it is also employed in making conductive polymers and batteries.

Three types of carbon black were used in this set of experiments. All samples were generously provided by Cabot Corporation. The brand names and APS‘s of the three samples are given below.

- Monarch 1300, with an APS of 9 nm
- Vulcan 9A32 with an APS of 20 nm
- Black Pearls 120 with an APS of 100 nm

4.2 First Carbon Black Experimental Setup

4.2.1 Sample Preparation

Ideally the carbon black would be deposited on a glass slides in a thin uniform coating. This presented a number of challenges. The problems associated with effectively dispersing nanotubes [63], graphene [64] and carbon black [65] are well documented. Two problems stand out. Due to their surface chemistry and large molecular weight, carbon microstructures are considered insoluble in all known solvents. Individual carbon black particles contain very little mass, consequently, the van der Waals forces acting between particles cause the carbon black particles to aggregate and makes them very difficult to effectively and evenly disperse.

Using a similar method devised to disperse SWNT's [66] and graphene [64] the carbon black was first mixed with anhydrous N,N-dimethylmethanamide (DMF). The solution was then immersed in a sonic bath for roughly 30 minutes. Several drops of this solution were then spin coated on to a glass slide spinning at 200 rpm. The samples were then investigated under a microscope. It was found that this method of deposition would yield small areas of even coating interspersed with areas of uneven, spotty and terraced coating, figure 4.1.

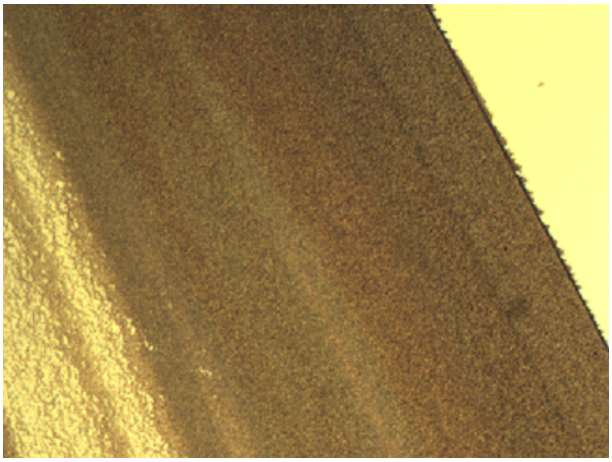

Fig. 4.1 Carbon black on a glass slide.

For the purpose of passing a small spot size beam through the carbon black, these samples were sufficient provided we could view the sample area being interrogated.

4.2.2 Imaging and Interrogating Setup

In order to measure the nonlinear optical absorption of the carbon black samples, an experimental setup was designed that would allow us to pass a tightly focused optical signal of known power through the sample and measure the power being transmitted and reflected. Assuming that losses due to scattering are minimal, the power absorbed is equal to the input power minus the reflected and transmitted power. By varying the input power we would expect to see a linear change in the reflected power and nonlinear change in the transmitted power in a sample that exhibits saturable absorption. As saturable absorption is a function of intensity, or power over area, a tightly focused signal allows for a higher intensity to input power ratio which is necessary given power limitations on the lasers used. CW signals have a constant

intensity, whereas pulsed sources carry power in high intensity pulses, this leads to pulsed sources having intensities that are orders of magnitude higher than CW sources of equal average power. Physical damage due to heating is generally a function of average power, as a result, materials with high saturation intensities can generally only be characterized with pulsed sources. Finally, the samples also needed to be imaged prior to interrogation in order to select a suitable target. The experimental setup is shown in figure 4.2

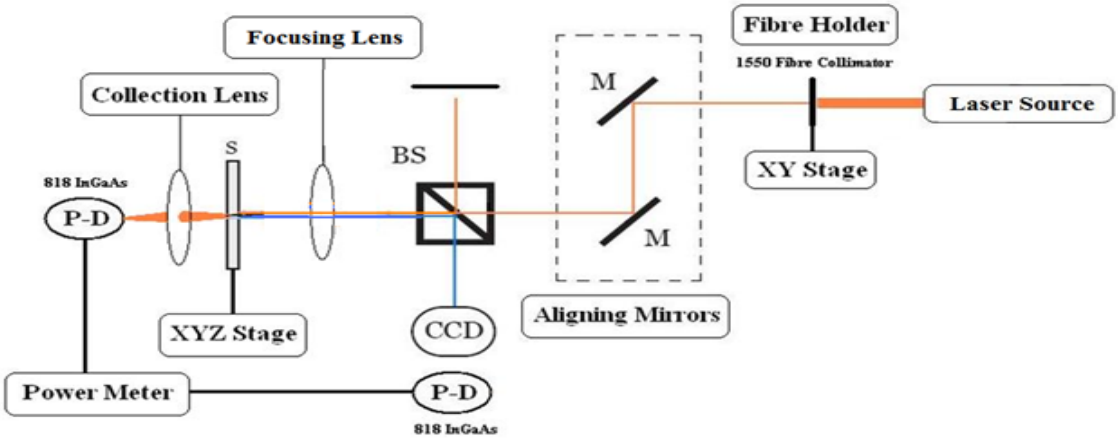

Fig. 4.2 Free space carbon black satureable absorption setup.

A 1550 nm collimating lens was placed on an XY stage in order to couple the signal into a set of alignment mirrors. The collimated signal was then passed through a 50/50 beam splitter and into an IR focusing lens set on an XY stage. The glass slide containing the sample was placed in a sample holder on an XYZ stage roughly in the focal plane of the focusing lens. Behind the sample, an IR collection lens was placed to focus the transmitted signal onto a photo detector (Newport 818-IR). By illuminating the sample from the backside with a lamp, and using the sample holder XYZ stage to bring it into the focus of the focusing lens, the sample could be imaged

through the beam splitter with a CCD camera. With the CCD camera removed, reflected power could be measured on a second photo detector. On the other side of the beam splitter in place of the beam blank, a photo detector could be used in order to monitor input power and used as a reference. The system was aligned both with a visible 632.8 nm Helium-Neon laser, and with a 1550 nm signal using an IR detection card.

4.2.3 Experimental Details

A sample was placed in the sample holder. Using a broadband lamp as an illumination device, the sample could be imaged on the IR sensitive CCD camera. A given point on the sample could then be identified as a suitable target area. By applying a weak CW 1550 nm signal at the source, the 1550 nm focus point could be precisely identified as the reflected light from glass slide would be visible with the CCD camera. By minimizing the spot size of the reflected signal we could ensure that as tightly focused a beam as possible would interrogate the sample. By placing an object of known size on a blank glass slide the spot size of the beam could be estimated. This setup allowed for the visualization of the sample and gave the ability to precisely aim the interrogating signal at a specific point as well as to control the focus of the signal.

There are two common approaches to performing a saturable absorption measurement, one is known as the z-scan. In a z-scan experiment, the interrogating signal is set to some arbitrarily high power. The target film is placed perpendicular to the z axis of the signal as illustrated in figure 4.3.

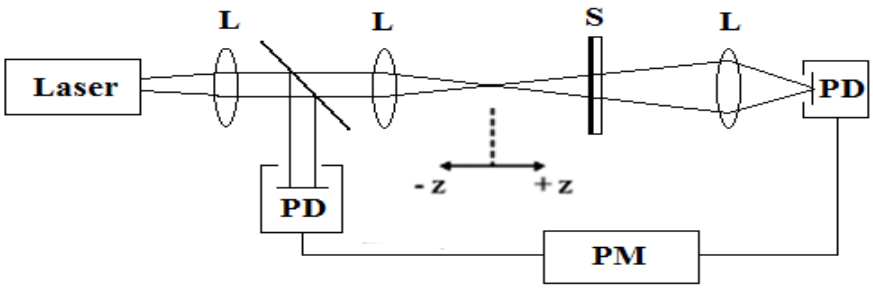

Fig. 4.3 Z-scan: Lens (L); Sample (S); Photo Detector (PD); Power Meter (PM).

As the sample is moved along the z axis, the beam either diverges or converges towards the beam waist. This has the effect of modulating the signal intensity (W/m^2) as the effective area of the spot size (m^2) changes while the signal power (W) remains constant. By monitoring the power in the transmitted beam, any changes in the sample absorption can be detected.

Although the setup that was built was ideally designed to perform this type of measurement, the sample preparation method was incapable of producing the large, evenly dispersed thin films required in order to accurately perform a z-scan. As the spot size increased and decreased it would incorporate areas of carbon black that were thicker and/or thinner than the original target area which would change the power being absorbed by the samples. This led to changes in the power throughput that were not due to any saturation in the absorption. The z-scan is an impractical measurement unless the sample depositions could be drastically improved.

The second method of measuring saturable absorption involves fixing the sample at the waist of the beam and varying the input power. By subtracting the transmitted power readings from the reference power, changes in the absorption or reflection can

be detected. By monitoring the reflected power changes in absorption can be isolated.

4.2.4 Continuous Wave Results

The samples were first interrogated using two laser sources at 1550 nm and at 1310 nm. The interrogation signals were generated by setting the laser source to its maximum value while controlling the output power using a variable optical attenuator (VOA). The samples were then selected and the signal was focused. The signal was then increased in half dB increments and the transmitted and reflected powers measured.

It was found that the power meters being used (Newport 2832-C and ILX Lightwave FPM-8200) did not have a linear response to input power. At every decade of input power, the internal integration time on the power meters would change, leading to sharp discontinuities in the power reading. As a result, when the transmitted power was subtracted from the reflected power in an attempt to identify the sample absorption, the result was a highly no-linear and discontinuous function of input power. The incurred error was judged to be too large to effectively identify a small change in the linear absorption.

To overcome this issue a second method was devised. A sample would be interrogated over a large range of input power values. A second measurement would then be performed by focusing the interrogating signal on a section of glass slide clean of carbon black or debris. A second VOA was introduced to mimic the linear absorption of the carbon black sample. By making a measurement over the same range of power inputs as the original sample measurement, the two measurements could be directly compared to determine if there was any nonlinear absorption in the sample. Reference value could still be collected as an additional control should they be necessary.

Measurements were conducted using various samples with both laser sources.

No saturable absorption was detected before the samples suffered from damage induced by high optical power inputs. It was observed that samples with larger areas of visibly flat carbon black deposits had a higher burn out threshold then smaller or more uneven surfaces. This was assumed to be due to the ease with which large homogeneous continuous samples could disperse heat. The highest optical power threshold observed without inducing permanent damage was 4 dBm of average power.

4.2.5 Pulsed Source Discussion and Results

As saturable absorption is a function of peak power, whereas damage is caused by an accumulation of average power, the decision was made to use a low duty cycle pulsed laser as an interrogating signal.

An ECL tuneable laser source set to 1550 nm was modulated using a pair of mach-zender electo-optic modulator (JDS Uniphase OC 192) being driven by a pulse generator. The pulses were amplifier using an EDFA. The pulses generated had a full width at half maximum (FWHM) of 1.5 ns, had a maximum average power of 6 dBm with a peak power of 450 mW and a repetition rate of 6 MHz. Despite the increase in peak power delivered by the pulsed source laser, no evidence of saturable absorption was detected before permanent damage was done to the samples.

Finally a Pritel Femtosecond Fiber Laser (FFL series) was obtained courtesy of Jose Azana at Institute National de la Recherche Scientifique (INRS). 2 picosecond pulsewidths were obtained with a repetition rate of 10 MHz, and an average power of around 1 dBm. This gives a peak power of around 75 W. Despite the increase in peak power delivered by the pulsed source laser, no evidence of saturable absorption

was detected.

4.3 Vacuum Carbon Black Experiments

Due to the sample burning, the saturable absorption measurement was next attempted in a vacuum environment, the theory being that a lack of oxygen would inhibit the burning of the carbon samples much like in a conventional incandescent light bulb. This would potentially allow for a significantly larger amount of power to be launched into the samples. The experiment involved depositing samples on a cleaved fiber tip and placing them inside a vacuum desiccator jar along with a photo detector. The desiccator would then be evacuated and the sample would be interrogated. Within an SMF 28 (single mode fiber) optical fiber light is tightly confined within the core of the fiber which has a diameter of roughly 8 μm. A benefit of this confinement was that we no longer needed to focus the light using a lens as was the case in the previous experiment. We also no longer needed to aim the signal as samples could be deposited directly on the fiber tip, covering the core, which also simplified the design. Apart from these two simplifications, the interrogation process generally remained the same. During the build up to the experiment a Calmar FPL-02cffPM mode-locked femtosecond laser was obtained by the Photonics Systems Group (PSG) at McGill, and for the remainder of the carbon black experiments, this laser was used. The Calmars central wavelength is 1550 nm, it has a pulse width of 700 fs, a repetition rate of 10 MHz and an average power output of 4 dBm. The peak power of the Calmar is roughly 150 W.

4.3.1 Sample Preparation

A cleaved bare fiber tip was immersed in the DMF carbon black solution. The tip was slowly withdrawn and allowed to dry in an upright position. The tips were then placed in a fiber holder and inspected under a microscope. Figure 4.4 below shows typical examples of the sample tips used for this set of experiments.

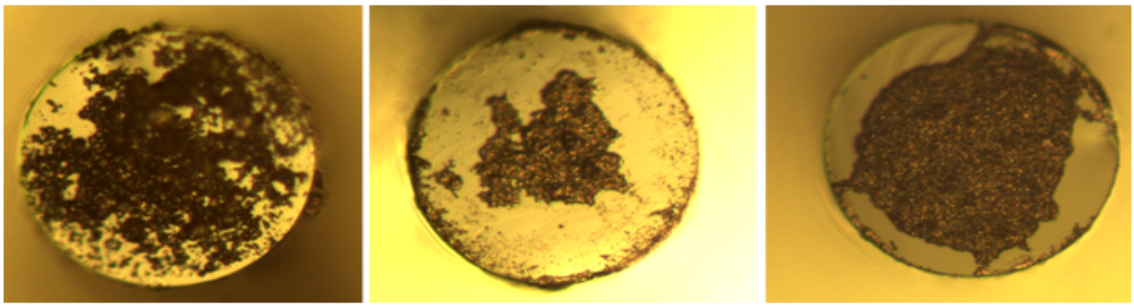

Fig. 4.4 A 9 nm APS covered tip, a 20 nm APS covered tip and a 100 nm APS covered tip.

The 9 nm carbon black proved to be the hardest to disperse in an even manner. Typically, the 9 nm carbon black would aggregate into balls on the order of several micrometers in diameter, and these balls would either remain isolated, or form uneven and porous stacks as is evident in the first picture in figure 4.4. Both the 20 nm and 100 nm carbon black could be made to cover the fiber core in an even manner. The vast majority of samples made using this dipping process were unusable. The three examples shown in figure 4.4 would be considered acceptable samples.

4.3.2 Vacuum Setup

The vacuum setup that was implemented is shown in figure 4.5.

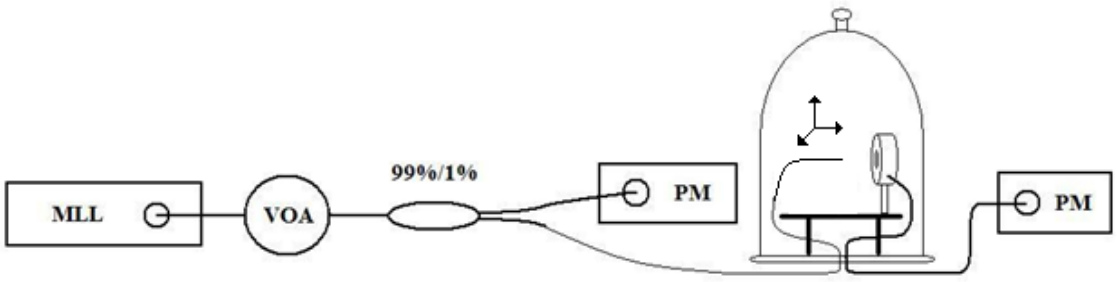

Fig. 4.5 First vacuum setup, power meter (PM)

A base for a desiccator jar was fabricated which incorporated a vacuum feedthrough to accommodate a KF 16 flange. A cross, having 4 flanges, was inserted into the base. One of the free flanges on the cross was used to connect a roughing pump and turbo pump vacuum system. The pressure was measured using a Pirani vacuum gauge fixed at the input to the turbo pump. Another flange connected to a BNC feedthrough, and the third flange was used to feed a stripped fiber into the desiccator. The fiber feedthrough was fabricated using a Swagelok connector flange and a Teflon cylinder with a #80 hole drilled through it [67]. The vacuum system was determined to have a base pressure on the order of a few mTorr.

A stand was fabricated to sit within the desiccator. Fixed to the stand was a fiber holder atop an XYZ stage. Next to the XYZ stage was a photo detector which was attached to the stand by means of an optical post.

The output of the MLL was feed into a high power VOA which was used to control the amount of power impinging on the sample. The 1% tap of a 99/1 beam splitter was used to monitor the power output of the VOA, while the 99% tap was feed into the desiccator jar through the vacuum feedthrough. The fiber tip containing the sample

was placed inside the desiccator in a fiber holder and aligned with a photo detector. The output of the photo detector was coupled out of the vacuum system though the BNC feedthrough and into a power meter.

Measurements were made in a similar way to the previously discussed method. A fiber tip containing a sample was placed in the fiber holder within the desiccator. The tip was positioned to be as close as possible to the photo detector. By applying a weak probe signal, the fiber tip was aligned with the photo detector by maximizing the power reading on the power meter. The desiccator was then sealed and pumped down to its base pressure. A measurement was made by slowly decreasing the attenuation on the VOA typically in increments of .5 to 1 dB, from 50 dB of attenuation down to 0 dB. Once a measurement was completed, the laser source was turned off and the vacuum chamber was allowed to return to atmospheric pressure. A calibrating measurement was then taken by cleaving the sample fiber tip, leaving a clean fiber face, and repeating the previous steps without a carbon sample. The VOA was given a slightly higher attenuation offset to mimic the linear attenuation of the carbon black sample. The two measurements were then compared to determine if there had been any saturation in the absorption.

4.3.3 Vacuum Experiment Results

The experimental results are shown in figures 4.6 and 4.7. All three sizes of carbon black showed an increase in transmission with increased input power. However, some important observations led to the conclusion that this was not in fact an electronic effect that would be expected in the case of a classic SA.

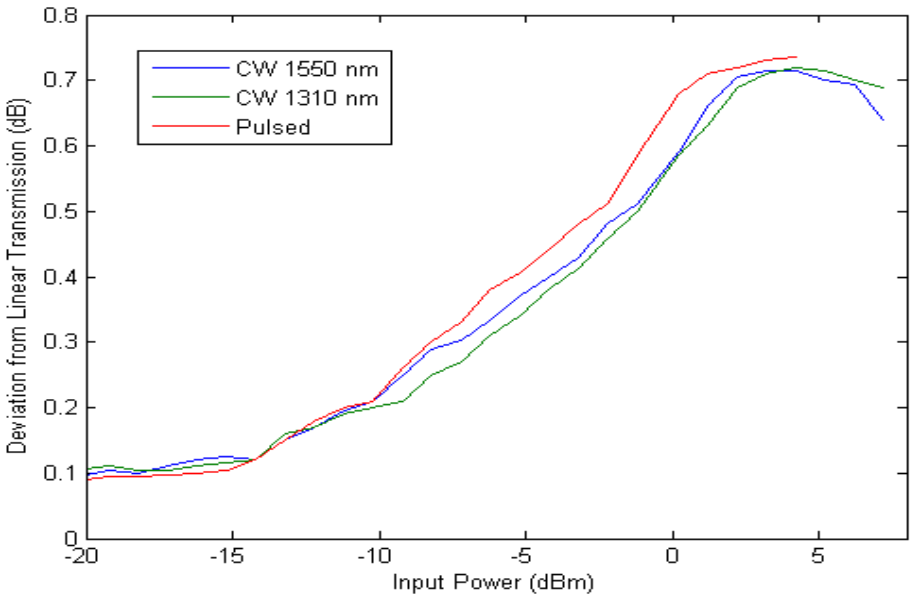

Fig. 4.6 Transmission vs input power for 100 nm APS, three sources.

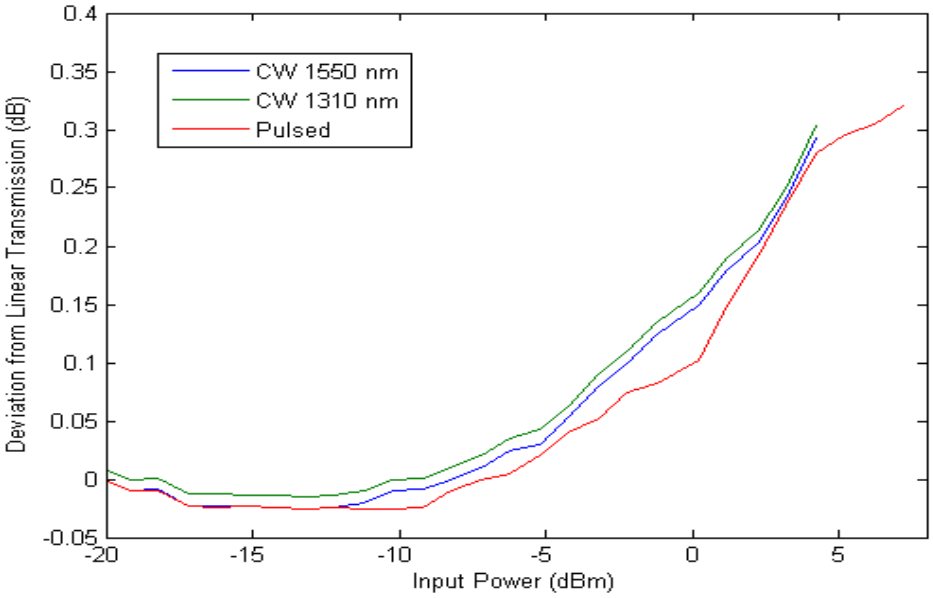

Fig. 4.7 Transmission vs input power for 20 nm APS, three sources.

The graphs were made by subtracting the output power measurements made with a clean cleaved fiber tip blank from the ones made with a carbon black covered tip.

The increase in transmission that was observed as the interrogation signal power was increased was observed to happen on a long time scale, on the order of tens of seconds. As an example, a low power signal was input to the sample and the attenuated output signal was measured on the power meter. If the input signal was then increased by 5 dB, the observed output signal would instantly increase by 5 dB and then continue to increase over time. Finally the output power reading would settle to some value that was greater than the 5dB increase in power applied at the input. In a similar vein, if the input power was then decreased by 5 dB, the transmitted power would then decrease by 5 dB and slowly continue to decrease before settling on the original power reading that was observed before the input power was changed. The transmission of the system was increasing, but at a rate much slower then would be expected as a classic SA response relies on electron-hole recombination, which takes place on a time scale of 100 ps to 100 fs.

The increase in transmission was not correlated to peak input power, but to average power. Each sample responded similarly to a pulsed source or a CW source as input. A classic SA should show a transmission characteristic that decreases with increasing peak power. The pulsed source used had a peak power many orders of magnitude higher than the CW signals used.

Many samples were tested, and certain patterns emerged. Samples with overall small signal absorption between 12 and 15 dB typically displayed the most pronounced nonlinearity. The transmission remained linear until around the -15 dBm to -10 dBm input power mark. Generally it was in this region that the transmission began to

increase. At around 3 to 7 dBm of input power, the transmission increase would begin to roll off, as can be seen clearly in figures 4.6 and 4.7. The power gap, expressed in dB, between the start of the nonlinearity and the roll off point seemed to remain relatively constant. The damage threshold for the samples was around 9 dBm. The maximum deviation from linear transmission that was observed was slightly greater the 1 dB as can be seen in the case of a 9 nm APS sample shown in figure 4.8. Samples that were reused on different days showed similar characteristics as long as they did not exceeded the damage threshold, indicating that the changes in transmission were not permanent.

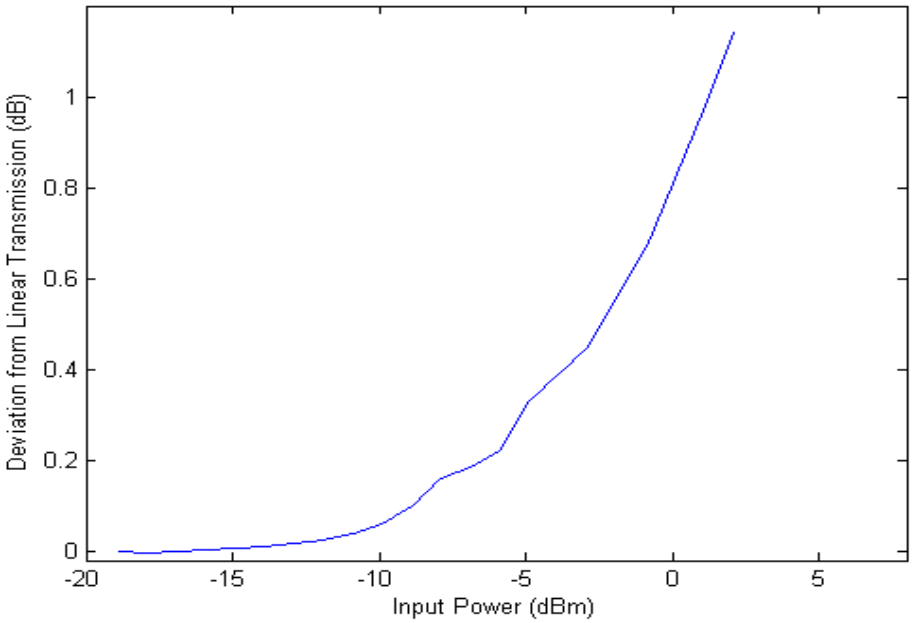

Fig. 4.8 Transmission vs input power for a 10 nm APS sample.

Two metrics can be used to quantify the samples, the APS and the amount of small signal absorption in the sample. The small signal absorption was measured by

measuring the output power of a fiber tip before and after a sample was deposited using the same power level. Neither of these factors could be correlated in any meaningful way to the variations in the data, including the start of the nonlinearity, the roll off point or the magnitude of the change.

4.3.4 Counter Propagating Vacuum Setup

To better understand the time dynamics of the effect being observed, a counter propagating pump-probe experiment was designed. The pump-probe consists of two signals, a high powered pump that is used to modulate the intensity of light in the sample, and a weak probe signal used to measure the change in the absorption. In a counter propagating configuration, the pump and probe pass through the sample in opposite directions, allowing for them to be independently measured. The advantage of the pump-probe is that the power in the probe remains constant and any change in absorption induced by the pump can be measured in real time.

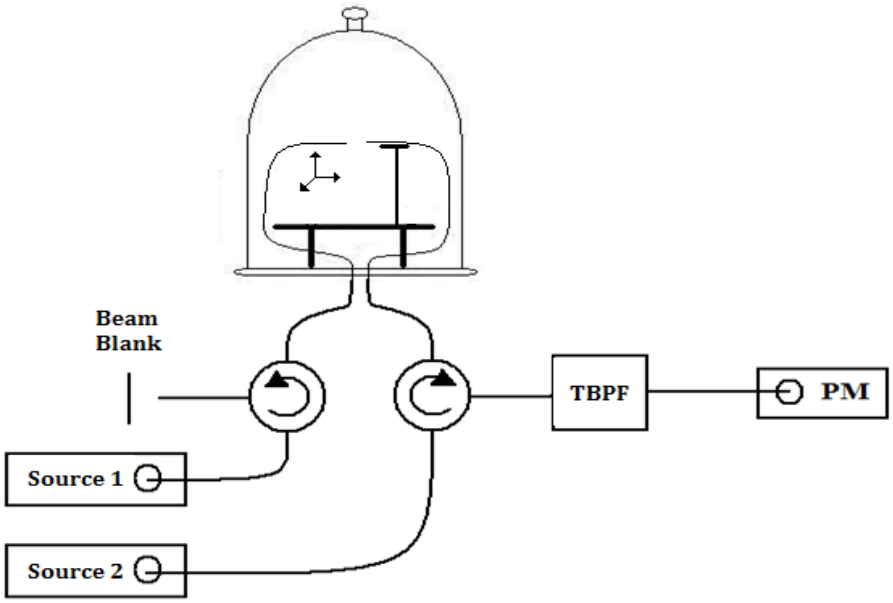

Fig. 4.9 Counter propagating vacuum setup

A pump probe type setup was devised to observe samples in vacuum, it is shown in figure 4.9. In this setup, source 1 is the probe signal, while source 2 is the pump. Source 1 is connected to a fiber optic circulator which feeds into the desiccator through a fiber feedthrough. The cleaved fiber tip of this branch holds the sample, it is known as the sample tip. It is held in place by a fiber holder set atop an XYZ stage. A second clean cleaved fiber tip, the collection tip, is help in place by a fixed fiber holder. This fiber leads out of the desiccator though a second fiber feedthrough and into a second optical circulator. Light entering the collection tip is directed out of the second circulator and through a tuneable notch filter into a power meter. Source 2 couples into the second circulator and is directed into the desiccator. To align the system, a low power signal is generated by source 1 and the sample tip is aligned with the collection tip using the XYZ stage until a maximum power output is read

on the power meter. The tuneable bandpass filter (TBPF) allows for the filtering out of any leakage from the pump signal in the second circulator or reflections from the face of the collection tip reaching the power meter assuming distinct pump and probe wavelengths. This was confirmed by applying a high power pump signal with no probe signal and observing the power reading on the power meter. The circulator in combination with the filter attenuates the pump signal by around 45 dB.

By using a low power CW probe signal at source 1, we can monitor changes in optical absorption of the sample by imputing a high power pump signal at source 2, and recording the power reading on the power meter.

4.3.5 Experimental Results

A sample was mounted in the desiccator and the system pumped down to base pressure. A weak probe signal was applied and the transmission of the probe measured in half second increments. A strong pump signal was then applied to the sample for some period of time before being turned off. The probe power was continuously measured. A typical measurement is shown in figure 3.10. For this measurement, a 1550 nm CW signal at -15 dBm was used as a probe, and a 0 dbm 1310 nm CW pump was used.

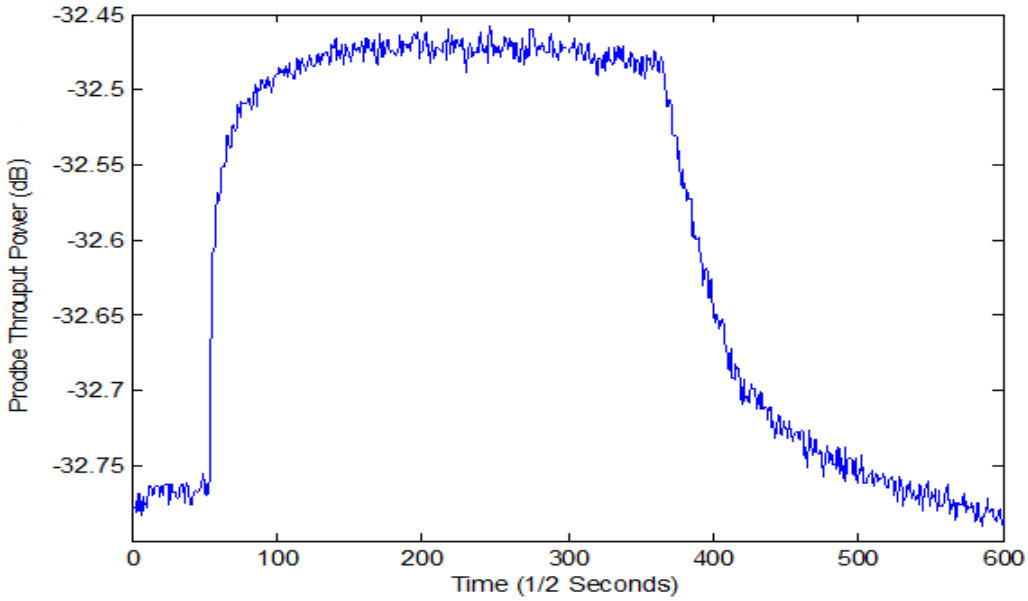

Fig. 4.10 Effect of a strong pump on the transmission of a weak probe signal over time.

In figure 4.10 we can clearly see the jump in transmission as the pump signal is applied. Initially the power meter reading is around -32.76 dBm. When the pump signal is applied the reading on the power meter increases with some time constant towards its final value of around -32.48 dBm, where it remains constant. The time required to come to steady state after the pump is turned on is around 40 seconds. Once the pump is turned off, the transmission then decreases back towards its original value of -32.76 dBm, requiring over a 100 seconds. The transmission increased by .3 dB due to the application of the counter propagating pump signal, and returned to its original value once the pump had been removed.

Several hypotheses were explored to explain this effect. One observation that was made during the set of vacuum experiments was that at sufficiently high input powers the carbon black sample would begin to emit light due to the heating effects of the

input signal. This was, in effect, an optically powered light bulb, similar in many ways to the incandescent light bulbs designed by Thomas Edison in the 1800's, who used electrically powered carbon filaments in vacuum. Knowing that the samples were being heated to thousands of degrees Kelvin, it was theorized that the carbon was emitting electrons due to thermionic emission, and that this reduction in electrons was resulting in a reduction in absorption. The long time constant can then be explained by noting that the samples were sitting on insulation glass which is surrounded by a non conducting polymer desiccator jar. Any escaping electrons would be slow to leave and slow to return. While this remains a possibility, it is perhaps not likely.

Another explanation which accounts for the long time constant has to do with a heating of the glass in the fiber. It was observed that the carbon black begins to emit light very quickly once a high power signal is applied, much faster than the change in transmission. This heat would then be transferred to the glass fiber, but at a much slower rate considering that glass is an effective thermal insulator. We do know that the index of refraction of the glass changes in response to a change of temperature as does its density and volume. This system is complicated by the fact that the higher index of refraction core is made of a doped glass whose doping characteristics are not readily available in the literature and are probably proprietary. Changes in index and volume could both affect the numerical aperture of the fiber, leading to an increase or decrease in the amount of light collected by the photo detector and collector tip. A simple model, whereby the heating effect increases the index of refraction equally in the core and cladding of the glass fiber leads to an increase in the numerical aperture, which leads to less light being collected by the photo detector, quite the opposite to what has been observed. Although this simple model gave a contrary results, heating

effects cannot be ruled out.

Unfortunately, both proposed explanations could not explain the effect being observed. This result might have been extremely useful were the transition to take place on a much faster time scale. If the origins of this effect could be isolated it might be possible to reduce the time constant to a point where it would have applications.

Finally, it remains a possibility that carbon black is a true saturable absorber, and that the slow saturation observed in these experiments effectively obscured a faster electronically induced saturation, as there was no way of distinguishing the two effects.

4.4 Electron Gun

As was previously mentioned, at sufficiently high pump input powers the carbon black sample heats up to the point where it begins to glow as a hot black body. An example of a glowing sample, pumped at 1310 nm, is shown in figure 4.11.

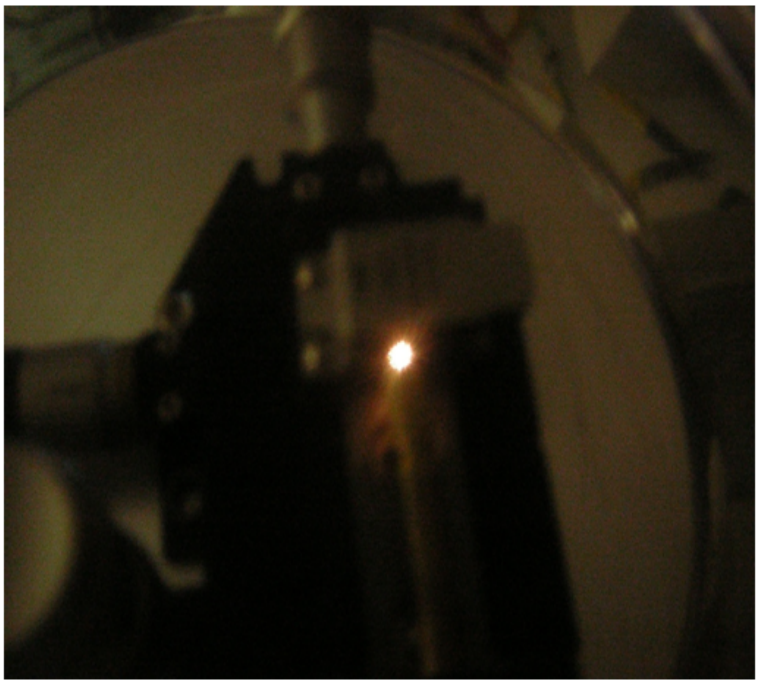

Fig. 4.11 Glowing sample.

This observation led to the idea that the carbon black and optical fiber tip combination could be, with some modification, turned into an optically pumped electron gun. Electron guns are used to produce a beam of electrons with precise kinetic energy. The most common application of the electron gun is the cathode ray tube, however they are also used in a number of other applications including electron microscopy, particle acceleration and, as is particularly relevant in this case, pulsed electron guns are used to build free electron lasers [11]. Typically electron guns are built with a hot cathode as a source and an anode that acts as a target. Electrons emitted by the source will accelerate in the electric field between cathode and anode. The principles of operation of an electron emitter are illustrated in figure 4.12.

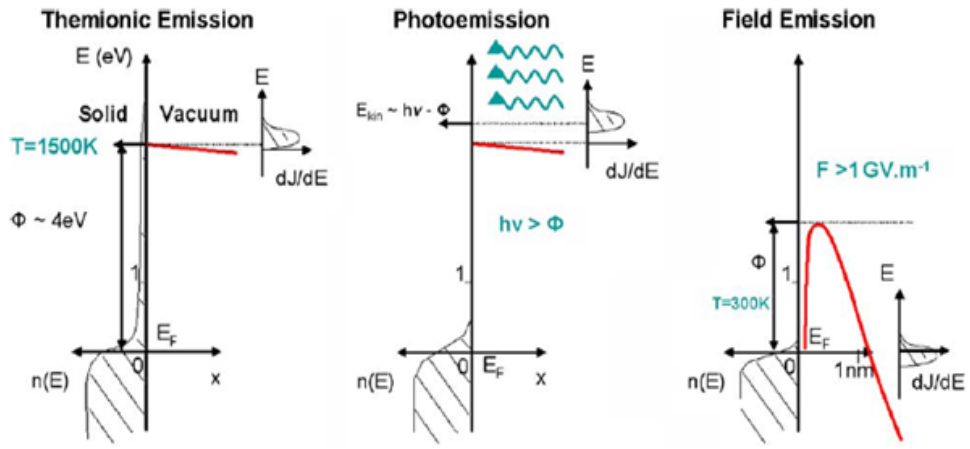

Fig. 4.12 Mechanisms for electron emission [11].

In photo assisted electron emission three mechanisms are employed to remove electrons from the source. Thermionic emission occurs as the source is heated to a sufficient temperature. With higher temperatures more electrons will find themselves in higher energy states within the Fermi distribution. An electron with a higher kinetic energy then the work function of the source material will be emitted by the cathode. Applying a potential between the cathode and anode not only gives the electrons a direction and acceleration, it also has the effect of lowering the sources work function, referred to as field emission. Photo emission is a result of the photoelectric effect, whereby an electron absorbs a photon resulting in the electron having a higher kinetic energy then the work function of the material, causing the electron to be emitted.

In order to turn a carbon black sample into a cathode, it needed to be electrically connected to an external source. With this in mind a number of bare fibres were coated with 100 nm of gold/palladium by vacuum sputtering. Once cleaved, the fiber tips had a conductive coating around the cladding but not on the face. By insuring

a carbon black sample deposited on the face touched the outside of the cladding an electrical connection was made. The anode was made out of a brass thumb tack. The full electrical connection to a source external to the desiccator was made though the BNC vacuum feedthrough previously engaged by the photo detector. The internal vacuum setup is shown in figure 4.13.

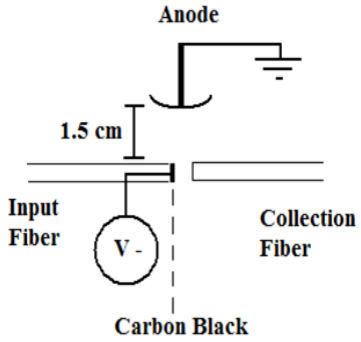

Fig. 4.13 Cathode and anode

A voltage was applied across the cathode anode junction and the output current was detected using a transconductance amplifier and a Keithly multimeter. The input power to the sample was provided by a DFB laser at 1310 nm. 1310 nm was used because of the high output power provided by the DFB laser, although 1550 nm gave the same effect. A plot of output current vs input power is shown in figure 4.14.

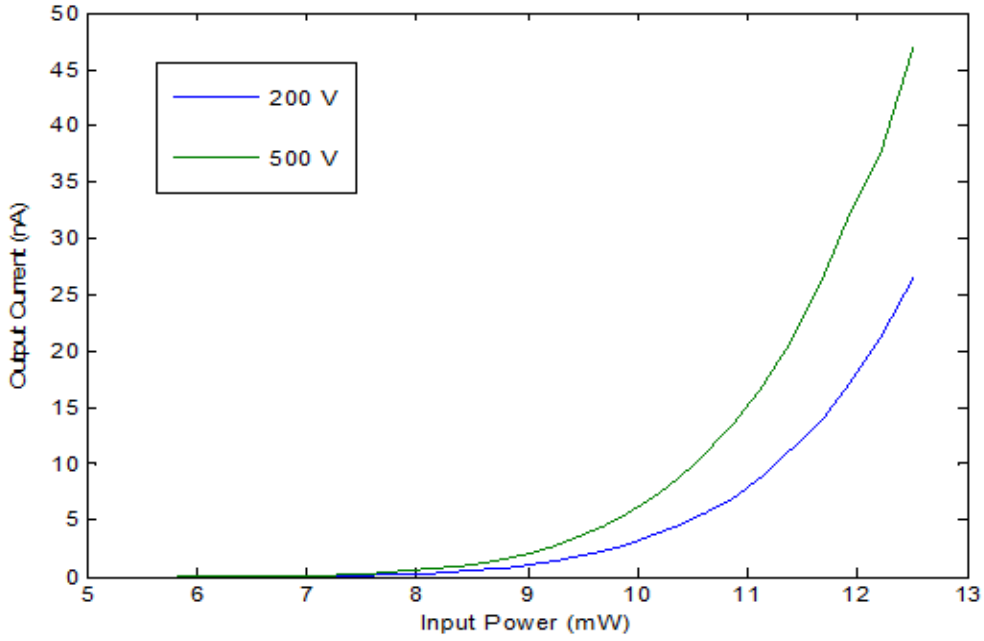

Fig. 4.14 Current drawn from a hot cathode at different bias voltages

The emission current density in a hot cathode field effect emitter can be modeled using the augmented Richards equation,

$$J(F,T,W) = A_G T^2 e^{((-(W-\triangle W))/kT)} \tag{4.1}$$

$$\triangle W = \sqrt{\frac{e^3 F}{4\pi\varepsilon_0}} \tag{4.2}$$

Where J is the current density ($\frac{A}{m^2}$), F is the field magnitude, T is the temperature in Kelvin, W is the work function of the material, k is the Boltzmann constant, ε_o is the vacuum permittivity and A_G is a material specific constant.

Although it would have been useful to fit equation 4.1 to the data obtained, and

determined what, if any, effect the photo electric effect had on the emission process, two major problems were encountered. First, a good determination of the temperature of the sample could have been obtained had it been possible to analyse the radiation emitted by the sample in a spectrum analyser and fitted this to a black body radiation curve. This would have been difficult as the sample was contained in the desiccator jar under vacuum. Secondly, there is inconsistency on the data available on the work function of carbon black.

A continuation of this set of experiments on the feasibility of optically pumped carbon black as an electron gun might be fruitful, however several improvements in equipment would be needed. Typical electron guns operate at much higher vacuum levels than can be achieved inside the desiccator [68], and facilities for obtaining a spectral measurement would be needed.

4.5 Ring Laser incorporating Carbon Black

Although we were unable to directly measure saturable absorption in carbon black in atmosphere, we did observe that the onset of mode-locking using CNT's occurred at a relatively low intensity, in the region of figure 3.4 where the nonlinear response is below the detection limit. It seemed possible that the carbon black might be a suitable material for mode-locking despite not having a measurable nonlinear response. With this in mind, experiments were performed whereby the carbon black was used in a fiber ring configuration, similar to the one use in chapter 3, in place of the CNT's in an attempt to demonstrate a pulsed laser source.

4.5.1 Experimental Setup

The carbon black was deposited onto the face of an APC fiber by dipping the fiber tip into dry carbon black. The fiber face was then examined using a microscope to ensure that a thin coating of carbon black covered the fiber core. The sample tip was then inserted into a fiber coupler to form a device similar to the one discussed in section 3.2 involving the carbon nanotubes. The carbon black containing device was then inserted into a fiber ring cavity as shown in figure 4.15.

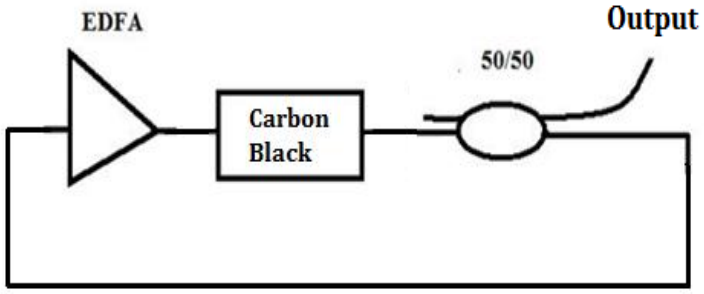

Fig. 4.15 Carbon black in a fiber ring laser.

The EDFA used was the preamplifier stage of a Pritel LNHPFA-33, and not the FA-18 used in the previous experiments. It should be noted that the EDFA contains an isolator ensuring that the cavity operates in a unidirectional manner. The output was observed using the same equipment as in the mode-locking experiments.

4.5.2 Experimental results

Time domain

The laser cavity showed a pulsed mode of operation as is shown in figure 4.16. The measurements were made at a number of intracavity powers and are unaveraged. Given that the laser output is coupled out of the cavity using a 50/50 coupler, the intracavity power at the coupler and the output power are equal, while the power hitting the carbon black will be around 4 dBm higher, that being the insertion loss of the carbon black device.

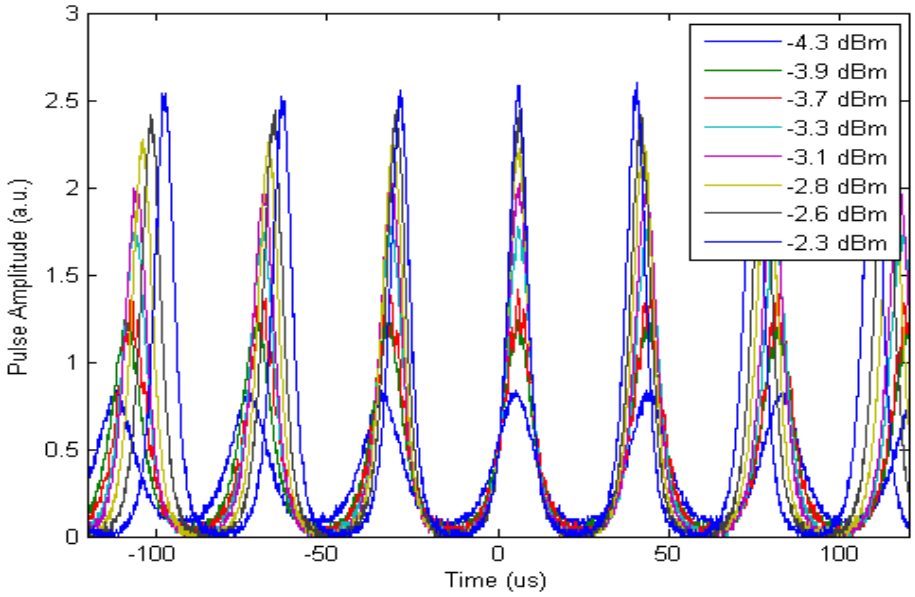

Fig. 4.16 Output pulses at various intracavity powers.

The laser begins to pulse at an EDFA pump current of around 42 mA, which corresponds to an output power of -4.3 dBm. At low pump current the laser operated in the CW regime.

The laser repetition rate was found to be power dependent and around 20 kHz, several orders of magnitude slower then the fundamental rep rate of the cavity, which is similar in length to the cavity used in the CNT MLL, having a fundamental frequency of around 10 MHz. Immediately we can conclude that the pulsed output is not due to mode-locking which would result in a rep rate equal to the fundamental cavity rate as was seen in chapter 3. We can also see that the pulse widths are on the order of microseconds and also appear to be power dependent. More will be said about the power dependent on the pulse characteristics in section 4.5.4.

Spectral Domain

The spectrum of the pulsed laser is shown in figure 4.17.

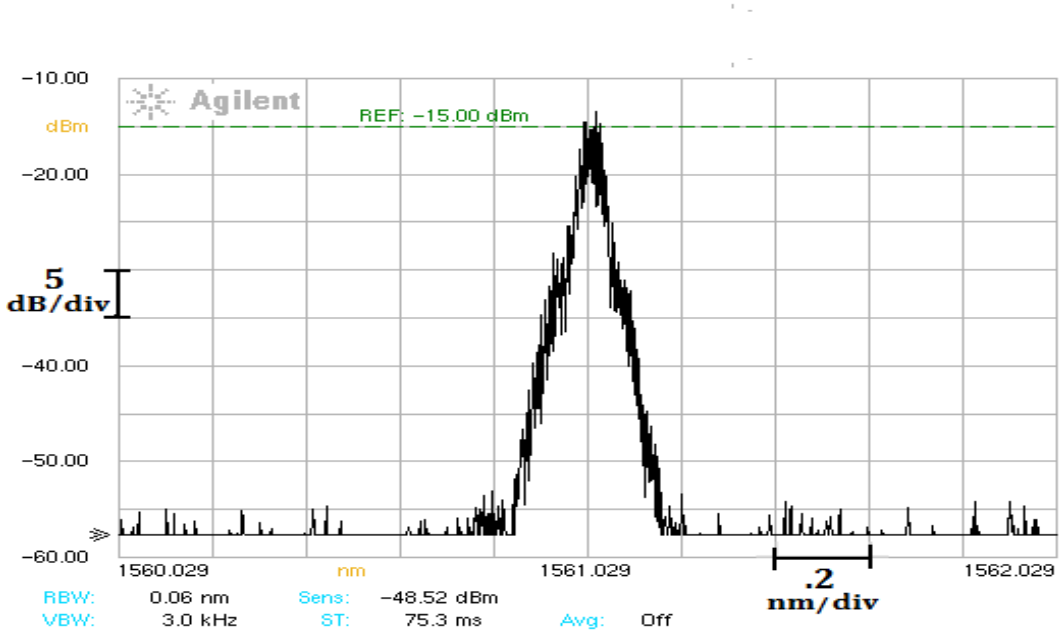

Fig. 4.17 Output in the spectral domain.

The output spectrum is that of a typical CW output at around 1561 nm. Given the broad pulse widths, on the order of microseconds, we would not expect to see bandwidth broadening. This output spectrum does not show any sign of mode-locking which would have a broad frequency content.

The pulse display the typical characteristics of a Q-switched laser. I will now briefly discuss Q-Switching before continuing to analyze the laser output in further detail.

4.5.3 Q-Switching

Passive saturable absorber Q-switching makes use of a SA within the laser cavity with a recovery time on the order of the lifetime of the gain medium. The excited lifetime of a typical EDFA is on the order of milliseconds. Q-switching was often observed in early laser systems involving SA dyes which have a long lived bleaching state. Today, Q-switching is a widely used technique for developing pulsed sources for use in range finding, laser cutting and drilling and for studying nonlinear optical effects due to the fact that the wide pulses developed by Q-switched lasers contain significantly more energy than mode-locked pulses.

The temporal dynamics of a passive Q-switched laser are shown schematically in figure 4.18.

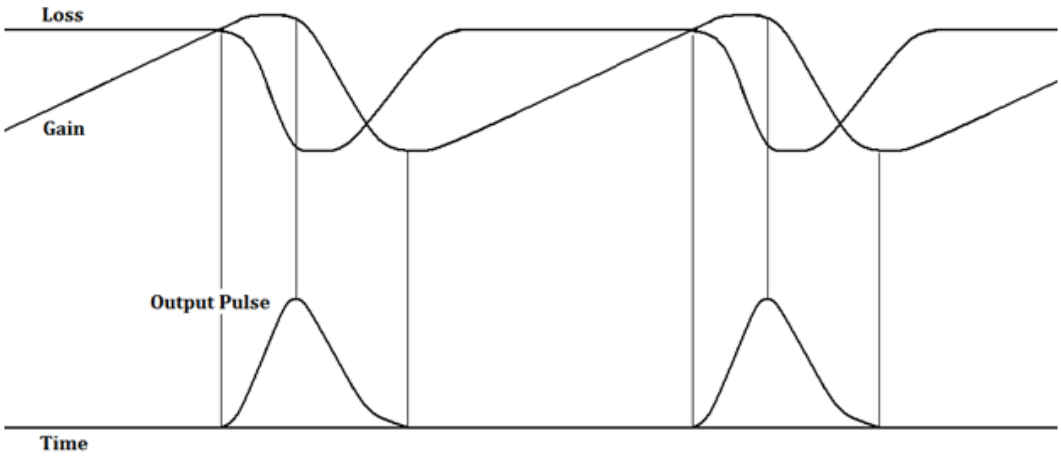

Fig. 4.18 Q-switching dynamics

When a laser gain medium is pumped, energy is stored within the medium in the form of excited states. The level of excitation corresponds to the population inversion, which corresponds to the system gain. A system will begin to lase when the level of gain is equal to the cavity losses.

Within the cavity of a Q-switched laser, the SA provides sufficient loss such that at low population inversion the system will not be lasing. This allows the population inversion to increase, storing energy within the cavity. As the level of gain surpasses the losses within the cavity the system begins to lase, and the power within the cavity increases. The intracavity power becomes sufficient to saturate the absorber, effectively changing the quality (Q) of the laser oscillator. With the reduced cavity loss, the power built up within the population inversion of the gain medium is quickly depleted, generating an output pulse. When the gain is sufficiently depleted, the intracavity power will no longer be sufficient to saturate the SA which begins to recover. If the loss recovers faster than the population inversion, then the process

will begin anew and the laser will repetitively Q-switch, developing a train of output pulses.

In contrast to mode-locking, the output repetition rate is not linked to the cavity length, but is determined by the lifetimes of the SA and the gain medium. The slope of the leading edge of the pulse is determined by the level of inversion of the gain medium, while the trailing edge is determined by the cavity decay rate. This often leads to asymmetric pulse shapes. It also leads to a pump power dependence on the pulse width and repetition rate. A more strongly pumped gain medium will emit more power, causing both the absorber and gain medium itself to saturate more quickly, which leads to shorter pulse widths and faster rep rates.

4.5.4 Laser Analysis

The rep rate, peak pulse power and pulse widths are all found to be power dependent. The power dependence of the rep rate is shown in figure 4.19.

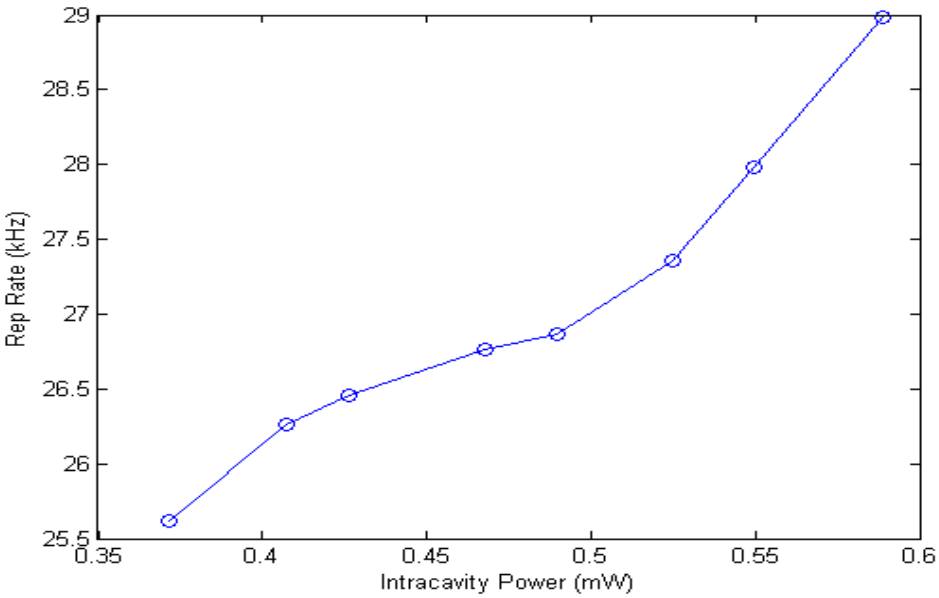

Fig. 4.19 Rep rate as a function of intracavity power.

As the intracavity power is increased, the rep rate of the laser also increases, which is typical of passively Q-switched lasers. The graph shows a general trend towards an accelerating rep rate as a function of power.

The peak power of the pulses as a function of output power is shown in figure 4.20.

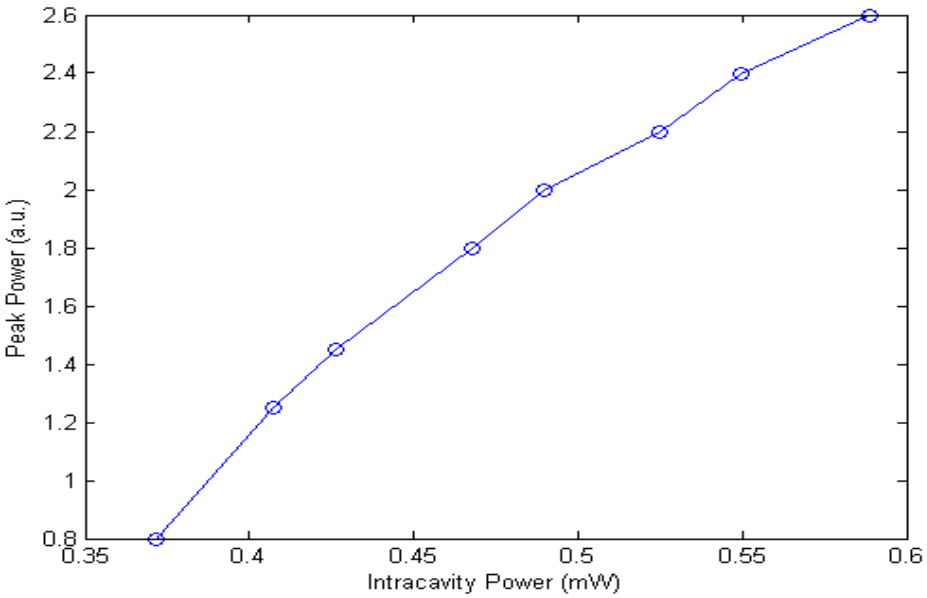

Fig. 4.20 Peak power as a function of output power.

As the pump power is increased the peak power of the pulses increases with a decreasing slope.

Because the Q-switched pulses are much longer in duration than the response time of the oscilloscope, the pulsewidth can be accurately measured without the use of an autocorrelator. The pulsewidth as a function of output power is shown in figure 4.21.

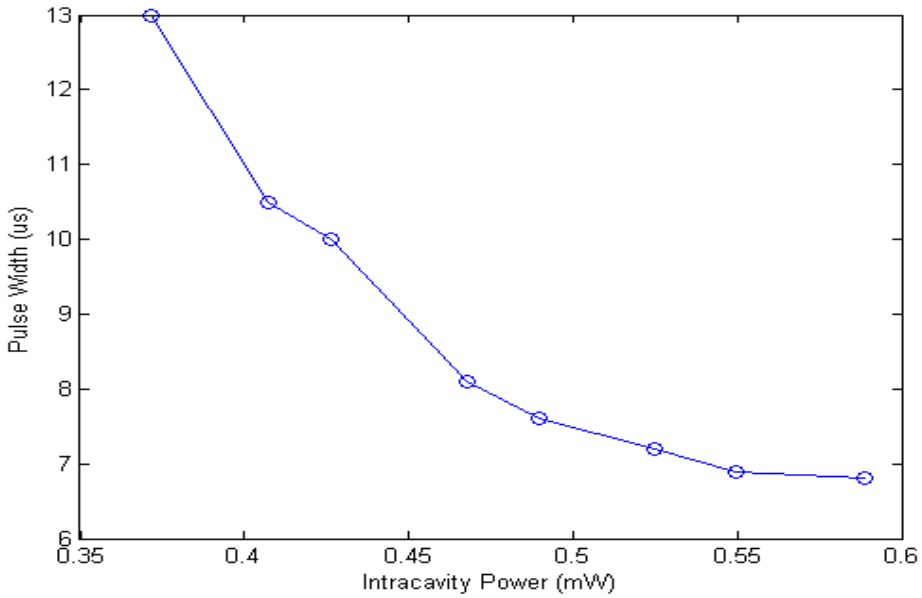

Fig. 4.21 Pulsewidth as a function of output power.

With increasing power, the pulse widths become shorter. The pulse widths appear to be reaching a minimum value of around 6 or 7 μs.

Considering the power dependences together, we can conclude that the pulse peak and width will eventually reach a steady state, at which point any additional intracavity power will cause an increase in frequency of the pulses.

The laser pulse characteristics are fully consistent with laser Q-Switching induced by a SA.

4.6 Cavity Tuneability and Power Output

Pulsed output was achieved using a variety of cavity configurations and components. The pulsed laser was found to be tuneable over the gain bandwidth of the EDFA by

inserting a .9 nm tuneable bandpass filter (TBPF) into the cavity as shown in figure 4.22.

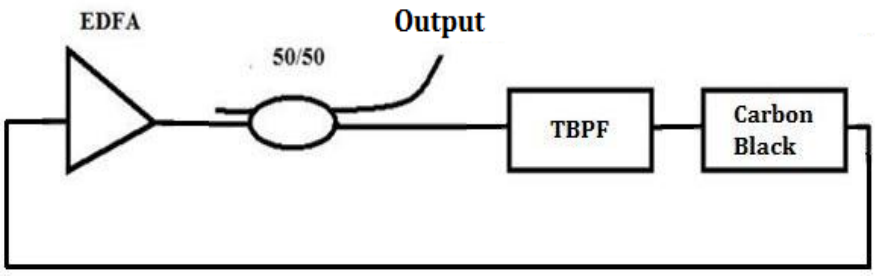

Fig. 4.22 Setup for tuneable high power output.

Figure 4.23 shows the spectrum at a number of wavelengths.

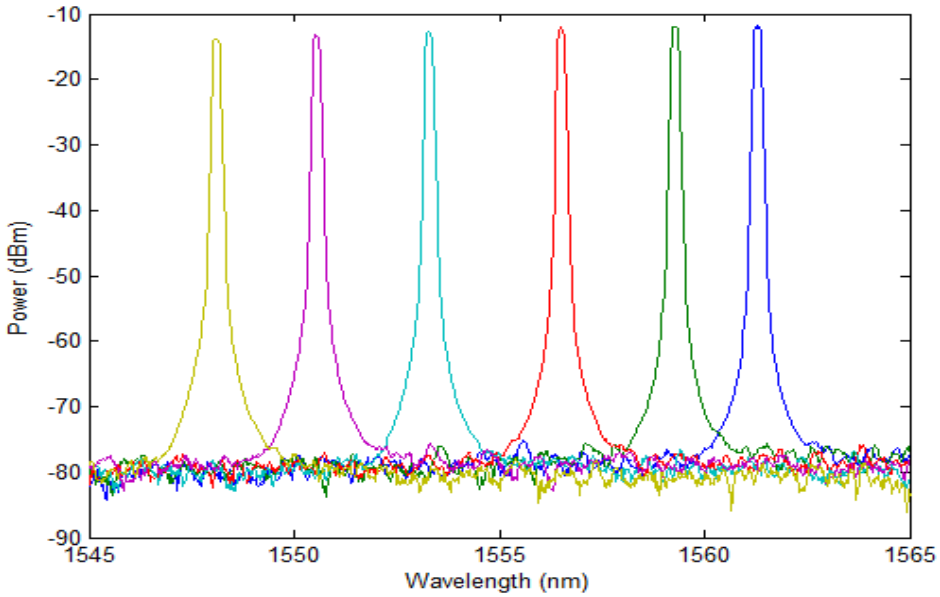

Fig. 4.23 Output in the spectral domain at various wavelengths.

The output power from the laser source could be maximized by placing the output coupler at the output of the EDFA, followed by the TBPF, followed by the carbon black device. In this configuration the majority of the power emitted by the EDFA is coupled out through the 50/50 coupler or blocked by the TBPF which has an insertion loss of around 5 to 6 dBm, before it is coupled into the carbon black device. This ensures that a minimum amount of power impinges on the carbon black. Average output powers in this configuration were found to be upwards of 8 dBm before noticeable damage was done to the carbon black. This corresponds to around 2 dBm of power hitting the carbon black sample at damage threshold which is consistent with previous measurements.

4.6.1 Q-Switching Conclusion

Examining the output of the laser cavity in figure 4.22 without the carbon black device present we observed a slightly modulated CW signal at low power. The modulation has a frequency on the order of microseconds and is comparable to the frequency of the fully Q-switched signal previously described. The origins of this modulation remains unidentified, but it is likely to be associated with parasitic reflection or nonlinearities within the wave division multiplexing (WDM) components or isolators within the EDFA. Pump power instability in the EDFA could also potentially cause output instability.

Although the signal modulation is present in the absence of the carbon black, the laser cavity does not display full Q-switching without the carbon black present.

We postulate that the Q-switching may arise from a combination of laser instability and a long recovery time saturation in the carbon black device, however, this remain

to be proven.

We can cite the saturation observed in vacuum previously described in section 4.3.3 of this chapter for some evidence that a saturation may be present, along with the effect seen in this laser system, as strong indications that carbon black does display some saturable absorption behaviour.

4.6.2 Future Work

An effort should be made to identify the specific origins of the observed Q-switching. The nature of the modulation instability in the EDFA, TBPF and coupler system should be identified. This will involve determining the components within the EDFA, and identifying any possible nonlinearity. The pump output would also need to be looked at to see if there is any identifiable fluctuation in pump power.

As for the pulsed source, a number of parameters need to be further studied. The peak power, pulse width and rep rate are all power dependent. A full characterization of these dependencies would need to be done. Looking at the effects of various cavity configurations as well as cavity length and linear loss within the cavity would also be of interest. In general looking at the power operating tolerances, including determining the damage threshold and lifetime for the carbon black samples, would need to be studied. Finally, looking at the wavelength tuneability and its effects on the laser output would also be useful.

4.7 Chapter Discussion and Conclusion

Although we were unable to find conclusive evidence for an optically induced saturable absorption consistent with the standard energy level model, as presented in the back-

ground, in the mid-IR for carbon black nanoparticles, a very slow nonlinear change in transmission with changes in input power was observed in vacuum. The time scale on which this change happens makes it unlikely to be due to energy level saturation which is expected to happen on a much shorter time scale. Moreover, the saturation that was observed was independent of peak power intensity; rather it was a function of average power input, which is not the case for the SA model of equation 2.6. The fact that the effect was observed only in vacuum would suggest a heating effect or gas absorption is a potential causes. We have also seen that the carbon black samples can be used to effectively Q-switch a laser, or at least amplify the laser instability seen in the Q-switching cavity. Both of these effects suggest that the carbon black exhibits a potential saturation. It remains possible that the saturation is a result of some interaction with the glass fiber.

Although we were unable to find any evidence for carbon black being an effective material for mode-locking of lasers, it remains possible that the carbon nanoparticles exhibit some true saturable absorption. As we have seen, as the layers of graphene increase the modulation depth of a graphene based SA's decreases dramatically. Assuming that the carbon black particles can be modeled as multiple sheets of graphene forming microcrystallite aggregations, we can assume that the larger the APS the smaller the modulation depth. A small modulation depth would be difficult to detect given the uncertainty with the measurement system used.

A continuation of vacuum experiment, where the saturation was observed, to determine the cause of the effect might be useful. A better method of sample deposition would be required, as knowing the width and dimensions of the sample would lead to a better understanding of the amount of heat built up in the sample and the fiber.

With a slight upgrade of the vacuum feedthrough design, it would be possible to control the specific gas within the desiccator. If the effect could be shown to be gas species dependent, this would indicate that change in absorption is due to some sort of carbon-gas interaction, however, at this point the mechanism remains unclear.

The photo assisted electron emitter shows some promise as a potential electron source due to its simplicity and low cost of fabrication. It might find applications, particularly in low temperature experiments where current consuming devices would be less ideal, or in pulsed source applications. Again, improved deposition would greatly assist in any further work, as the size and position of the sample on the fiber face would have an impact on the current being drawn. An upgrade of the vacuum system would also be needed to increase the electric field strength and improve the device lifetimes.

The Q-switched laser source shows some promise as a pulsed laser source. Although the specifics of the pulse development are not fully understood, it is both cheap and very simple to implement. With further study, it may be possible to develop the laser source into a useful tool given that the pulse width, peak power and rep rate are all tuneable. A continuation of this set of experiments would be easily done using the equipment available in the lab.

Chapter 5

Conclusion

In chapter 3 we built and characterized a fiber ring laser which used CNT's as a passive mode locking SA element and an EDFA gain element. The laser generated pulses on the order of 1 ps pulsewidth at 10 MHz with a 3 dB bandwidth of 3.5 nm. The power circulating within the laser cavity was determined to comprise of dispersion managed solitons pulses. The laser rep rate was found to be pump power dependent and could be increased in a harmonic fashion, with a maximum rep rate of 130 MHz. The damage threshold for the CNT's was determined to be around 7 dBm, at which point the linear absorption increased while the saturable absorption was found to decrease. After the SA had been optically damaged, the laser cavity was found to generate bound soliton pairs.

Chapter 4 comprised an attempt to determine whether carbon black nanoparticles exhibit any nonlinear optical response. Although the results were inconclusive, a long lived nonlinear response was observed in carbon black on optical fiber in vacuum. Further work would be needed in order to identify the specific origins of this phenomenon. The carbon black on optical fiber device was also determined to be an

effective electron emitter when placed inside a vacuum jar. Finally, a passively Q-switched fiber ring laser incorporating carbon black was built and characterized. The laser was found to exhibit typical Q-switched behaviour including power dependent pulsewidth, rep rate and peak power. The laser was found to be tuneable over a 20 nm range, centered at 1555 nm.

References

[1] H. Haus, "Mode-locking of lasers," *Selected Topics in Quantum Electronics, IEEE Journal of*, vol. 6, no. 6, pp. 1173 –1185, nov. 2000.

[2] K. F. Mak, M. Y. Sfeir, Y. Wu, C. H. Lui, J. A. Misewich, and T. F. Heinz, "Measurement of the optical conductivity of graphene," *Phys. Rev. Lett.*, vol. 101, no. 19, p. 196405, Nov 2008.

[3] O. Jost, A. A. Gorbunov, W. Pompe, T. Pichler, R. Friedlein, M. Knupfer, M. Reibold, H.-D. Bauer, L. Dunsch, M. S. Golden, and J. Fink, "Diameter grouping in bulk samples of single-walled carbon nanotubes from optical absorption spectroscopy," *Applied Physics Letters*, vol. 75, no. 15, pp. 2217 –2219, oct. 1999.

[4] Q. Bao, H. Zhang, Y. Wang, Z. Ni, Y. Yan, Z. X. Shen, K. P. Loh, and D. Y. Tang, "Atomic-layer graphene as a saturable absorber for ultrafast pulsed lasers," *Advanced Functional Materials*, vol. 19, 2009.

[5] S. Y. Set, H. Yaguchi, Y. Tanaka, and M. Jablonski, "Laser mode locking using a saturable absorber incorporating carbon nanotubes," *J. Lightwave Technol.*, vol. 22, no. 1, p. 51, 2004. [Online]. Available: http://jlt.osa.org/abstract.cfm?URI=JLT-22-1-51

[6] J. M. Dawlaty, S. SHivaraman, M. Chandrashekhar, F. Rana, and M. G. Spencer, "Measurement of ultrafast carrier dynamics in epitaxial graphen," *Appl. Phys. Lett.*, vol. 92, no. 4, 2008.

[7] A. Schmidt, S. Rivier, G. Steinmeyer, J. H. Yim, W. B. Cho, S. Lee, F. Rotermund, M. C. Pujol, X. Mateos, M. Aguiló, F. Díaz, V. Petrov, and U. Griebner, "Passive mode locking of yb:kluw using a single-walled carbon nanotube saturable absorber," *Opt. Lett.*, vol. 33, no. 7, pp. 729–731, 2008. [Online]. Available: http://ol.osa.org/abstract.cfm?URI=ol-33-7-729

[8] T. Cabioch, J. C. Girard, M. Jaouen, M. F. Denanot, and G. Hug, "Carbon onions thin film formation and characterization," *Europhys. Lett.*, vol. 38, no. 9, pp. 471–475, 1997.

[9] A. G. Rozhin, Y. Sakakibara, S. Namiki, M. Tokumoto, H. Kataura, and Y. Achiba, "Sub-200-fs pulsed erbium-doped fiber laser using a carbon nanotube-polyvinylalcohol mode locker," *Appl. Phys. Lett.*, vol. 88, no. 5, 2006.

[10] D. V. Khudyakov, A. S. Lobach, and V. A. Nadtochenko, "Passive mode locking in a ti:sapphire laser using a single-walled carbon nanotube saturable absorber at a wavelength of 810 nm," *Opt. Lett.*, vol. 35, pp. 2675–2677, 2010.

[11] R. Ganter, R. Bakker, C. Gough, M. Paraliev, M. Pedrozzi, F. L. Pimpec, L. Rivkin, and A. Wrulich, "Nanosecond field emitted and photo-field emitted current pulses from zrc tips," *Nuclear Instruments and Methods in Physics Research*, vol. 65, pp. 423–429, 2006.

[12] P. T. Guerreiro, S. Ten, N. F. Borrelli, J. Butty, G. E. Jabbour, and N. Peyghambarian, "Pbs quantum-dot doped glasses as saturable absorbers for mode locking of a cr:forsterite laser," *Applied Physics Letters*, vol. 71, no. 12, pp. 1595 –1597, sep. 1997.

[13] D. H. Sutter, G. Steinmeyer, L. Gallmann, N. Matuschek, F. Morier-Genoud, U. Keller, V. Scheuer, G. Angelow, and T. Tschudi, "Semiconductor saturable-absorber mirror assisted kerr-lens mode-locked ti:sapphire laser producing pulses in the two-cycle regime," *Opt. Lett.*, vol. 24, no. 9, pp. 631–633, 1999. [Online]. Available: http://ol.osa.org/abstract.cfm?URI=ol-24-9-631

[14] A. J. DeMaria, D. A. Stetser, and H. Heinan, "Diode-end-pumped passively mode-locked high-power nd:yvo4 laser with a relaxed saturable bragg reflector," *Opt. Lett.*, vol. 26, pp. 199 –201, 2001.

[15] F. Seguineau, D. Rouvillain, P. Brindel, H. Choumane, G. Aubin, J.-L. Oudar, B. Lavigne, and O. Leclerc, "Regeneration capabilities of passive saturable absorber-based optical 2r in 20gbit/s rz dwdm long-haul transmissions," in *Conference on Lasers and Electro-Optics/Quantum Electronics and Laser Science Conference*. Optical Society of America, 2003, p. CThX3. [Online]. Available: http://www.opticsinfobase.org/abstract.cfm?URI=CLEO-2003-CThX3

[16] D. Massoubre, J.-L. Oudar, A. O'Hare, M. Gay, L. Bramerie, J.-C. Simon, A. Shen, and J. Decobert, "Analysis of thermal limitations in high-speed microcavity aturable absorber all-optical switching gates," *J.*

Lightwave Technol., vol. 24, no. 9, p. 3400, 2006. [Online]. Available: http://jlt.osa.org/abstract.cfm?URI=JLT-24-9-3400

[17] S. Y. Set, H. Yaguchi, M. Jablonski, Y. Tanaka, Y. Sakakibara, A. G. Rozhin, M. Tokumoto, H. Kataura, Y. Achiba, and K. Kikuchi, "A noise suppressing saturable absorber at 1550nm based on carbon nanotube technology," in *Optical Fiber Communication Conference*. Optical Society of America, 2003, p. FL2. [Online]. Available: http://www.opticsinfobase.org/abstract.cfm?URI=OFC-2003-FL2

[18] H. W. Mocker and R. J. Collins, "Mode competition and self-locking effects in a q-switched ruby laser," *Appl. Phys. Lett.*, vol. 7, 1965.

[19] A. J. DeMaria, D. A. Stetser, and H. Heinan, "Self mode locking of lasers with saturable absorbers," *Appl. Phys. Lett.*, vol. 8, 1966.

[20] J. A. Valdmanis, R. L. Fork, and J. P. Gordon, "Generation of optical pulses as short as 27 femtoseconds directly from a laser balancing self-phase modulation, group-velocity dispersion, saturable absorption, and saturable gain," *Opt. Lett.*, vol. 10, no. 3, pp. 131–133, 1985. [Online]. Available: http://ol.osa.org/abstract.cfm?URI=ol-10-3-131

[21] U. Keller, K. J. Weingarten, F. X. Kartner, D. Kopf, B. Braun, I. D. Jung, R. Fluck, C. Honninger, N. Matuschek, and J. A. der Au, "Semiconductor saturable absorbers mirrors for femtosecond to nanosecond pulse generation in solid-state lasers," *IEEE J. Sel. Top. Quantum Electron.*, vol. 2, 1996.

[22] K. Mansour, M. J. Soileau, and E. W. V. Stryland, "Nonlinear optical properties of carbon-black suspensions (ink)," *J. Opt. Soc. Am. B*, vol. 9, no. 7, pp. 1100–1109, 1992. [Online]. Available: http://josab.osa.org/abstract.cfm?URI=josab-9-7-1100

[23] H. Haus, "Theory of mode locking with a fast saturable absorber," *J. Appl. Phys.*, vol. 46, no. 7, pp. 1063 –1073, 1975.

[24] R. Kroto H.W.and Heath J.R.and Brien S.C.and Curl R.F.and Smalley, "C60: Buckminsterfullerene," *Nature*, vol. 318, pp. 162 –163, 1985.

[25] S. Iijima, "Helical microtubules of graphitic carbon," *Nature*, vol. 354, pp. 56–57, 1991.

[26] K. S. Novoselov, A. K. Geim, S. V. Morozov, D. Jiang, Y. Zhang, S. V. Dubonos, I. V. Grigorieva, and A. A. Firsov, "Electric Field Effect in Atomically Thin Carbon Films," *Science*, vol. 306, no. 5696, pp. 666–669, 2004.

[27] K. S. Novoselov, A. K. Geim, S. V. Morozov, D. Jiang, M. I. Katsnelson, I. V. Grigorieva, S. V. Dubonos, and A. A. Firsov, "Two-dimensional gas of massless dirac fermions in graphene," *Nature*, vol. 438, no. 10, pp. 197–200, 2005.

[28] R. R. Nair, P. Blake, A. N. Grigorenko, K. S. Novoselov, T. J. Booth, T. Stauber, N. M. R. Peres, and A. K. Geim, "Fine Structure Constant Defines Visual Transparency of Graphene," *Science*, vol. 320, no. 5881, pp. 1308–, 2008.

[29] F. Wang, A. Rozhin, Z. Sun, V. Scardaci, R. Penty, I. White, and A. Ferrari, "Fabrication, characterization and mode locking application of single-walled carbon nanotube/polymer composite saturable absorbers," *International Journal of Material Forming*, vol. 1, pp. 107–112, 2008, 10.1007/s12289-008-0371-y. [Online]. Available: http://dx.doi.org/10.1007/s12289-008-0371-y

[30] R. Setton, P. Bernier, and S. Lefrant, *Carbon molecules and materials*. London and New York: Taylor and Francis, 2002.

[31] T. Schibli, K. Minoshima, H. Kataura, E. Itoga, N. Minami, S. Kazaoui, K. Miyashita, M. Tokumoto, and Y. Sakakibara, "Ultrashort pulse-generation by saturable absorber mirrors based on polymer-embedded carbon nanotubes," *Opt. Express*, vol. 13, no. 20, pp. 8025–8031, 2005. [Online]. Available: http://www.opticsexpress.org/abstract.cfm?URI=oe-13-20-8025

[32] Y.-W. Song, S. Yamashita, C. S. Goh, and S. Y. Set, "Passively mode-locked lasers with 17.2-ghz fundamental-mode repetition rate pulsed by carbon nanotubes," *Opt. Lett.*, vol. 32, no. 4, pp. 430–432, 2007. [Online]. Available: http://ol.osa.org/abstract.cfm?URI=ol-32-4-430

[33] Z. Sun, A. G. Rozhin, F. Wang, T. Hasan, D. Popa, W. O'Neill, and A. C. Ferrari, "A compact, high power, ultrafast laser mode-locked by carbon nanotubes," *App. Phys. Lett.*, vol. 95, 2009.

[34] A. Schmidt, S. Rivier, G. Steinmeyer, J. H. Yim, W. B. Cho, S. Lee, F. Rotermund, M. C. Pujol, X. Mateos, M. Aguiló, F. Díaz, V. Petrov, and U. Griebner, "Passive mode locking of yb:kluw using a single-walled carbon nanotube saturable absorber," *Opt. Lett.*, vol. 33, no. 7, pp. 729–731, 2008. [Online]. Available: http://ol.osa.org/abstract.cfm?URI=ol-33-7-729

[35] M. A. Solodyankin, E. D. Obraztsova, A. S. Lobach, A. I. Chernov, A. V. Tausenev, V. I. Konov, and E. M. Dianov, "Mode-locked 1.93 μm thulium fiber laser with a carbon nanotube absorber," *Opt. Lett.*, vol. 33, no. 12, pp. 1336–1338, 2008. [Online]. Available: http://ol.osa.org/abstract.cfm?URI=ol-33-12-1336

[36] F. Wang, A. G. Rozhin, V. Scardaci, Z. Sun, F. Hennrich, I. H. White, W. I. Milne, and A. C. Ferrari, "Wideband-tuneable, nanotube mode-locked, fibre laser," *Nature Nanotechnology*, vol. 3, pp. 738–742, 2008.

[37] F. Bonaccorso, Z. Sun, T. Hasan, and A. C. Ferrari, "Graphene photonics and optoelectronics," *Nature*, vol. 4, pp. 611–622, 2010.

[38] D.-P. Zhou, L. Wei, B. Dong, and W.-K. Liu, "Tunable passively q-switched erbium-doped fiber laser with carbon nanotubes as a saturable absorber," *IEEE Photonics Technology Letters*, vol. 22, no. 1, pp. 9–11, 2010.

[39] J. W. Nicholson, R. S. Windeler, and D. J. DiGiovanni, "Optically driven deposition of single-walled carbon-nanotube saturable absorbers on optical fiber end-faces," *Opt. Express*, vol. 15, no. 6, pp. 9176–9183, 2007.

[40] *Corning SMF-28 Optical Fiber, Product Information*, 2002. [Online]. Available: http://www.corning.com/WorkArea/showcontent.aspx?id=27659

[41] A. Hasegawa and F. Tappert, "Transmission of stationary nonlinear optical physics in dispersive dielectric fibers i: Anomalous dispersion," *Appl. Phys. Lett.*, vol. 23, no. 4, pp. 171–172, 1973.

[42] L. F. Mollenauer, R. H. Stolen, and J. P. Gordon, "Experimental observation of picosecond pulse narrowing and soliton in optical fibers," *Phys. Rev. Lett.*, vol. 45, no. 13, pp. 1095–1098, 1980.

[43] G. P. Agrawal, *Lightwave Technology, Telecommunication systems.* Hoboken N. J.: Wiley Interscience, 2005.

[44] G. L. Lamb, *Ultrafast optics.* New York, N. Y.: Wiley Interscience, 1980.

[45] N. N. Akhmediev and A. Ankiewicz, *Dispersive Solitons.* New York, N. Y.: Springer, 1980.

[46] A. M. Weiner, *Ultrafast optics.* Hoboken N. J.: Wiley Interscience, 2008.

[47] S. M. J. Kelly, "Characteristc sideband instability of periodically amplified average soliton," *Appl. Phys. Lett.*, vol. 28, no. 8, pp. 806–807, 1992.

[48] D. J. Jones, Y. Chen, H. A. Haus, and E. P. Ippen, "Resonant sideband generation in stretched-pulse fiber lasers," *Appl. Phys. Lett.*, vol. 23, no. 19, pp. 1535–1537, 1998.

[49] W. S. Man, H. Y. Tam, M. S. Demokan, and D. Y. Tang, "Soliton shaping of dispersive waves in a passively mode-locked fiber ring laser," *Opt. and Quant. Elect.*, vol. 33, pp. 1139–1147, 2001.

[50] S. T. Cundiff, B. C. Collings, N. N. Akhmediev, J. M. Soto-Crespo, K. Bergman, and W. H. Knox, "Observation of polarization-locked vector solitons in an optical fiber," *Phys. Rev. Lett.*, vol. 82, no. 20, pp. 3988–3991, May 1999.

[51] C. Pare and P.-A. Belanger, "Spectral domain analysis of dispersion management without averaging," *Opt. Lett.*, vol. 25, no. 12, pp. 881–883, 2000.

[52] N. Akhmediev, "Dynamics of solitonlike pulse propagation in birefringent optical fiber," *Phys. Rev. E*, vol. 49, no. 6, pp. 5742–5754, 1994.

[53] A. B. Grudinin, D. J. Richards, and D. N. Payne, "Energy quantisation in figure eight fiber laser," *Elec. Lett.*, vol. 28, no. 1, pp. 67–68, 1992.

[54] V. J. Matsas, T. P. Newman, D. J. Richards, and D. N. Payne, "Selfstarting passively mode-locked fiber ring soliton laser exploiting nonlinear polarisation rotation," *Elec. Lett.*, vol. 28, no. 15, pp. 1391–1393, 1992.

[55] F. Salin, P. Grangier, and A. Brun, "Experimental observation of nonsymetric n=2 solitons in femtosecond laser," *Phys. Rev. Lett.*, vol. 60, no. 7, pp. 569–572, 1988.

[56] M. J. Lederer, B. Luthers-Davies, H. H. Tan, C. Jagadish, N. N. Akhmediev, and J. M. Soto-Crespo, "Multipulse operation of a ti:sapphire laser mode locked by an ion-implanted semiconductor saturable-absorber mirror," *J. Opt. Soc. Am. B*, vol. 16, no. 6, pp. 895–904, 1999.

[57] D. Y. Tang, H. Zhang, L. M. Zhao, and X. Wu, "Observation of high-order polarization-locked vector solitons in a fiber laser," *Phys. Rev. Lett.*, vol. 101, no. 15, p. 153904, Oct 2008.

[58] D. Y. Tang, L. M. Zhao, B. Zhao, and A. Q. Liu, "Mechanism of multisoliton formation and soliton energy quantization in passively mode-locked fiber lasers," *Phys. Rev. A*, vol. 72, no. 4, pp. 043 816–1–9, 2005.

[59] E. Wolf, *Progress in optics, volume 48*. Amsterdam: Elsevier, 2005.

[60] B. A. Malomed, "Bound soliton in the nonlinear schrodinger-ginzburg-landau equation," *App. Phys. A*, vol. 44, no. 10, pp. 6954–6957, 1991.

[61] D. Y. Tang, B. Zhao, D. Y. Shen, and C. Lu, "Compound pulse solitons in a fiber ring laser," *Phys. Rev. A*, vol. 68, pp. 013 816–1–8, 2003.

[62] D. Y. Tang, L. M. Zhao, and B. Zhao, "Multipulse bound solitons with fixed pulse separations formed by direct soliton interaction," *App. Phys. B*, vol. 80, pp. 239–242, 2005.

[63] S. B. Sinnott and R. Andrews, "Carbon nanotubes: Synthesis, properties, and applications," *Critical Reviews in Solid State and Materials Sciences*, vol. 26, pp. 145–249, 2001.

[64] Y. Hernandez, V. Nicolosi, M. Lotya, F. M. Blight, Z. Sun, S. De, I. T. McGovern, B. Holland, M. Byrne, Y. K. Gunko, J. J. Boland, P. Niraj, G. Duesberg, S. Krishnamurthy, R. Goodhue, J. Hutchison, V. Scardaci, A. C. Ferrari, and J. N. Coleman, "High-yield production of graphene by liquid-phase exfoliation of graphite," *Nature Nanotechnology*, vol. 3, pp. 563–568, 2008.

[65] H. G. Kilian, "Carbon blacks as dissipative colloid systems with universal properties," *Colloid Polym Sci*, vol. 280, pp. 661–673, 2002.

[66] C. A. Furtado, U. J. Kim, H. R. Gutierrez, L. Pan, E. C. Dickey, and P. C. Eklund, "Debundling and dissolution of single-walled carbon nanotubes in amide solvents," *J. AM. CHEM. SOC*, vol. 126, pp. 6095–6105, 2004.

[67] E. R. I. Abraham and E. A. Cornell, "Teflon feedthrough for coupling optical fibers into ultrahigh vacuum systems," *Applied Optics*, vol. 37, pp. 1762–1763, 1998.

[68] L. Reimer, *Scanning electron microscopy, physics of image formation and microanalysis*. New York, N. Y.: Springer, 1998.